Accelerator design report for 3-GeV Next-Generation Synchrotron Radiation Facility

September 2020

National Institutes for Quantum and Radiological Science and Technology (QST)

Institute for Advanced Synchrotron Light Source

This design report outlines the current accelerator design of 3NGSR (3-GeV Next-Generation Synchrotron Radiation) facility at the Aobayama new campus of Tohoku University. This facility is expected to form a National photon science platform together with SPring-8, which covers a wide spectral range from UV to hard X-rays. The 3NGSR facility mainly provides long-wavelength lights ranging from UV to tender X-rays. The 3NGSR facility is therefore required to be a practical SX (Soft-X-ray) light source with high performance, stability and reliability.

As another aspect, the 3NGSR construction project has faced a quite tight budget, human resources, and time schedule. In order to fit the severe conditions, we have designed the accelerator complex with strong supports from RIKEN, JASRI, and KEK accelerator-groups and have extensively introduced outcomes from R&D and design studies for SPring-8-II.

The accelerator design has the following features:

1. target emittance set around 1nm.rad giving a high coherence at SX wavelengths
2. compact ring design based on quintet bend achromat with combined bends
3. 3-GeV C-band full-energy linac injector enabling a future extension to SX FEL (Free Electron Laser)

At last, we would like to express grateful thanks to all the collaborators from QST, RIKEN, JASRI, and KEK accelerator groups for their tremendous contributions, and also to give appreciations to directors, administrative staffs, and all the involved persons in the above laboratories.

Representatives of QST Accelerator Group
Nobuyuki Nishimori, Takahiro Watanabe, and Hitoshi Tanaka

Contents

1. Lattice

1.1 Storage ring lattice

When MAX Laboratory of Sweden introduced a so-called multi-bend achromat lattice with seven bending magnets per cell for the new 3 GeV light source, MAX IV, in pursuit of low-emittance rings with the emittance of lower than 1 nm rad, it was nothing short of an epoch-making undertaking. Natural or horizontal emittance is theoretically reduced in inverse proportion to the cube of the number of bending magnets, which makes multi-bend configuration is essential for lowering the emittance. This, however, makes the packing factor of the magnet arrangement extremely high, making it difficult to arrange other accelerator components such as gate valves, beam diagnostic instruments, and so on. Lowering the emittance also demands multipole (quadrupole and sextupole) magnetic fields that are significantly stronger than the conventional levels. It inevitably requires decreasing a bore diameter of each multipole magnet that makes the beam duct narrower, and conductance smaller, causing difficulties in designing the vacuum system. Despite these difficulties, most of the upgrading plans for existing synchrotron radiation facilities use this multi-bend lattice, and it is bound to become even more common in the light source ring lattice.

The storage ring has also employed a type of multi-bend lattice called double double-bend achromat (DDBA) lattice, which has 4 bending magnets per cell. With its 16 cells, the designed storage ring has a horizontal emittance of 1.14 nm rad and a circumference of 349 m. While DDBA is a type of multi-bend lattice, the number of its bending magnets is not extremely large as with MAX IV's 3 GeV ring, and the resulting emittance is therefore not as small. Even so, the design allows for a compact cell structure, making it possible to achieve the lower emittance than that of a current third-generation light source with a relatively short circumference.

Table 1.1 shows the key parameters of the storage ring. A DDBA unit cell is comprised of four bending magnets, ten quadrupole magnets, ten sextupole magnets used for the linear chromaticity correction and the nonlinearity suppression, and orbit-correction dipole magnets. Each cell is 21.8-m long. Of the sixteen 5.4-m long straight sections, fourteen are for installing undulators and the remaining two are for beam injection systems and radiofrequency (RF) accelerating cavities. As for the 1.6-m short straight sections, fourteen have multipole wigglers (MPWs) that generate high-intensity white-light hard X-rays in lieu of bending magnets, and the other two have a beam instability suppression system, beam diagnostic instruments, a beam current monitor (DCCTs), beam collimators, and so on.

Table 1.1 Key parameters of the storage ring

Beam energy	E	2.998 GeV
Lattice structure		Double Double-Bend Achromat
Circumference	C	348.843 m
Number of cells (bends)	N_{cell}	16 (64)
Long straight section	LSS	5.44 m × 16
Short straight section	SSS	1.64 m × 16
Betatron tune	(ν_x, ν_y)	(28.17, 9.23)
Natural chromaticity	(ξ_x, ξ_y)	(-60.50, -40.99)
Natural horizontal emittance	ε_x	1.14 nmrad
Momentum compaction factor	α_0	0.00043
Natural energy spread	σ_E/E	0.0843 %
Lattice function at LSS	$(\beta_x, \beta_y, \eta_x)$	(13.0, 3.0, 0.0) m
Lattice function at SSS	$(\beta_x, \beta_y, \eta_x)$	(4.1, 3.0, 0.05) m
Damping partition number	(J_x, J_y, J_e)	(1.389, 1.0, 1.611)
Damping time	(τ_x, τ_y, τ_e)	(8.1, 11.2, 7.0) ms
Energy loss in bends	U_0	0.621 MeV/turn
RF accelerating frequency	f_{RF}	508.759 MHz
RF accelerating voltage	V_{RF}	3.6 MV
Harmonic number	h	592
Natural bunch length	σ_b	2.92 mm (9.74 ps)

The linear optics is an achromatic design with an energy-dispersion function of zero for each long straight section. Figure 1.1 shows the distribution of lattice functions along the unit cell.

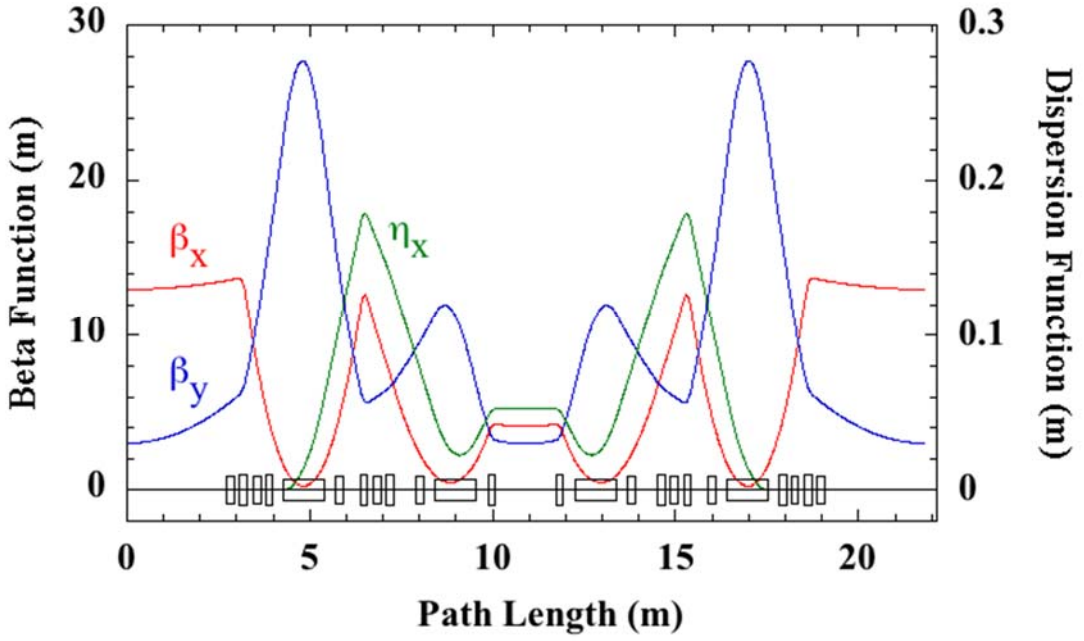

Figure 1.1 Distribution of lattice functions along the unit cell. The red and blue lines represent horizontal and vertical β functions, respectively, and the green line represents the horizontal energy dispersion function.

As a bending magnet, a combined-function-type electromagnet that combines the dipole magnetic field with the quadrupole one is used in order to make the ring small and reduce the horizontal emittance. The dipole magnetic field is 0.87 T to reduce the radiation loss per turn, so that the power consumption by the RF cavities is reduced. The combined quadrupole field is 7.06 T/m. For the quadrupole and sextupole magnets the maximum strengths are 49 T/m and 1541 T/m^2, respectively, which are achievable with a realistic bore diameter and the effective length is 20 cm for all these magnets. Table 1.2 shows the specifications of these electromagnets and figure 1.2 shows the magnet lattice of the unit cell.

Table 1.2 Specifications of main electromagnets

Magnet	Name	Length (m)	Strength (T, T/m, T/m^2)
Combined Dipole	B	1.13	0.8688, 7.06
Quadrupole	Q1	0.20	+32.6151
	Q2	0.20	-2.6278
	Q3	0.20	+49.1523
	Q4	0.20	+5.4300
	Q5	0.20	+44.6423
Sextupole	S1	0.20	+949.50
	S2	0.20	-1124.87
	SD1	0.20	-472.34
	SF	0.20	+1061.73
	SD2	0.20	-1540.68

Although the drift spaces between Q3 and B and between Q4 and B are relatively large in the magnet lattice shown in Fig. 2.2, this is intended to make the dispersion peak larger in the dispersion arc and reduce the SF strength (no phase matching is carried out for the purpose of making the sextupole magnetic fields transparent, however). Beta function distortions caused by MPWs installed in the short straight sections, along with the tune shifts, are corrected using trim coils attached to upstream Q1 and downstream Q5 in combination with main power supplies.

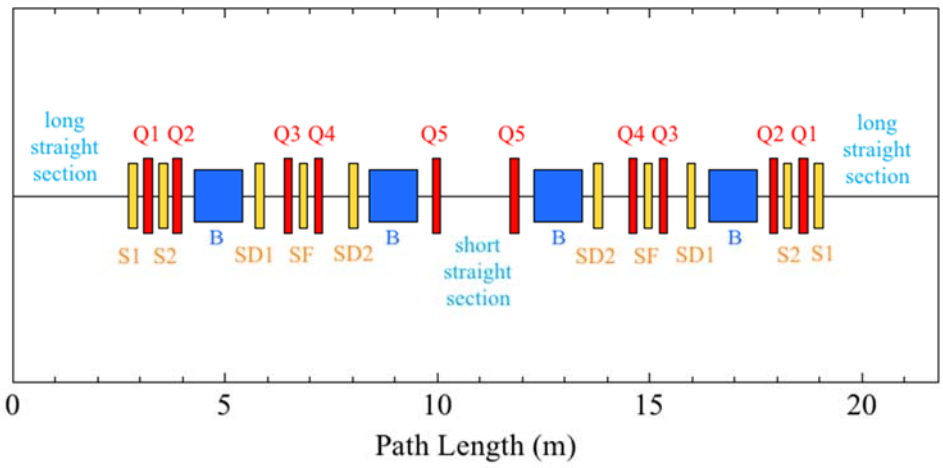

Figure 1.2 Magnet lattice of the unit cell. Blue: bending magnets (1 family); red: quadrupole magnets (5 families); yellow: sextupole magnets (5 families).

1.2 Electron beam dynamics in storage ring

1.2.1 Optimization of sextupole magnetic field strengths to expand dynamic aperture

As expected from the lattice of the storage ring, the linear chromaticity is corrected with SF, SD1 and SD2. Because the dynamic aperture (DA) of the ring varies depending on the SD1-SD2 balance, and the optimization of the distribution of sextupole magnetic strengths was carried out to maximize the dynamic aperture, including the strengths of S1 and S2.

The target chromaticity was set at (+1, +1); 3.6-MV RF accelerating voltage was applied in order to take account of a synchrotron oscillation of tracking particles with energy deviations (off-momentum particles). Figure 1.3 shows the DAs obtained at the center of the long straight section. Even with energy deviations of ±3%, a horizontal aperture of approximately -15 mm is secured, which is large enough for the stable beam injection. In the vertical direction, an aperture of 7 mm is obtained and this value is smaller compared with the horizontal one. However, it is not a serious problem because the minimum operating gaps of the in-vacuum undulators are planned to be around 5 mm.

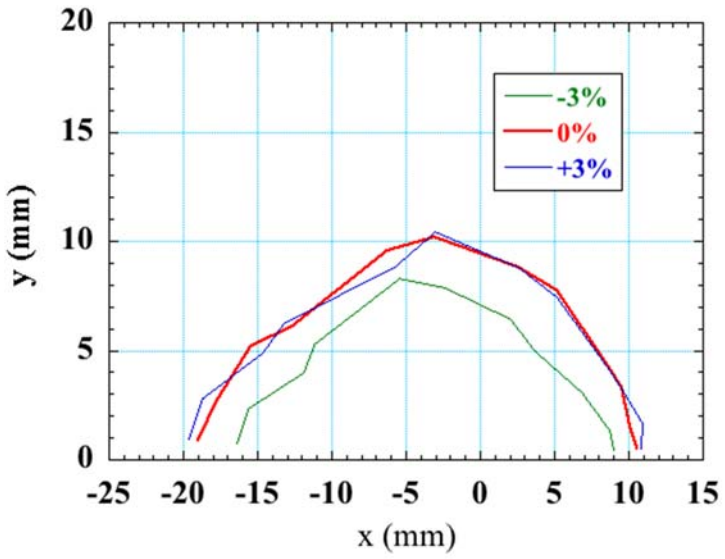

Figure 1.3 DAs for on-momentum particles at the center of the 5.4-m long straight section and for off-momentum particles with energy deviations of ±3%. Operating point: (ν_x, ν_y) = (28.17, 9.23).

The maximum value of sextupole magnetic field strengths is 1541 T/m^2 , a level attainable using a bore diameter of 40 mm. Figure 1.4 shows the dependence of tunes on the momentum deviation (a) and the horizontal and vertical oscillation amplitudes (b, c).

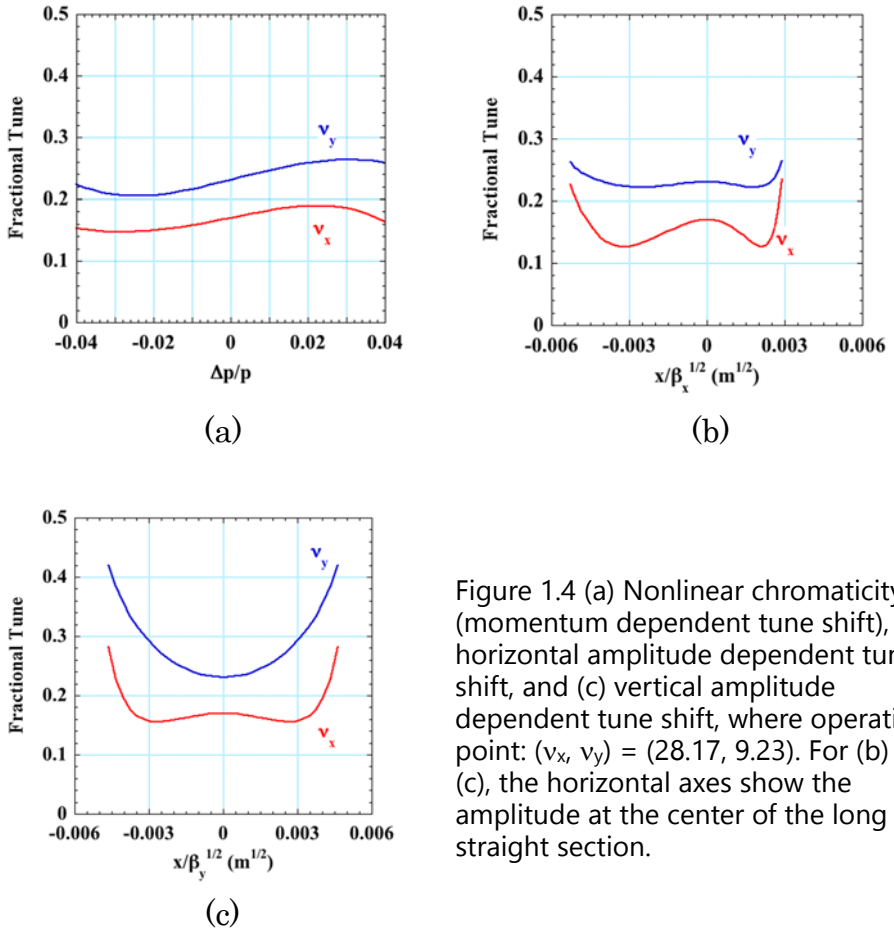

Figure 1.4 (a) Nonlinear chromaticity (momentum dependent tune shift), (b) horizontal amplitude dependent tune shift, and (c) vertical amplitude dependent tune shift, where operating point: (ν_x, ν_y) = (28.17, 9.23). For (b) and (c), the horizontal axes show the amplitude at the center of the long straight section.

In a range where a normalized momentum deviation changes form -3% to +3% the tune shift is kept approximately less than 0.1. This shows that the nonlinear chromaticity is well suppressed by the optimization in this range. On the other hand, as seen in Fig. 1.4, the amplitude dependent tune shift seems to be rather large even in the required amplitude range. However, under the condition that the excitation of several resonance lines nearby the operating point is properly controlled by the optics correction procedures and magnet error tolerances, the amplitude dependent tune shifts obtained do not affect the stable beam operation.

1.2.2 Momentum aperture and Touschek lifetime

Momentum aperture (MA) can be kept sufficiently by applying established correction procedures, such as COD, tune, and beta function corrections, under allowable magnetic errors. To evaluate the Touschek lifetime, the local MA distribution in a regular cell was calculated conservatively, using the following conditions: (1) 31 points at the edge of bending and quadrupole magnets are selected as evaluation points for each cell; (2) random alignment errors of sextupole magnets (σ = 25 μm with a cut-off at 2σ) are assumed; (3) an RF accelerating voltage is 3.6 MV; (4) synchrotron oscillation is taken into account without radiation losses; and (5) insertion devices are not considered in the simulation model. Figure 1.5 shows the simulation result. Absolute MAs are between 3% and 5% in terms of normalized momentum deviation ($\Delta p/p$), and it strongly correlates with the horizontal dispersion. Mean MA values are +4.1% for the positive $\Delta p/p$ side and -4.4% for the negative $\Delta p/p$ side.

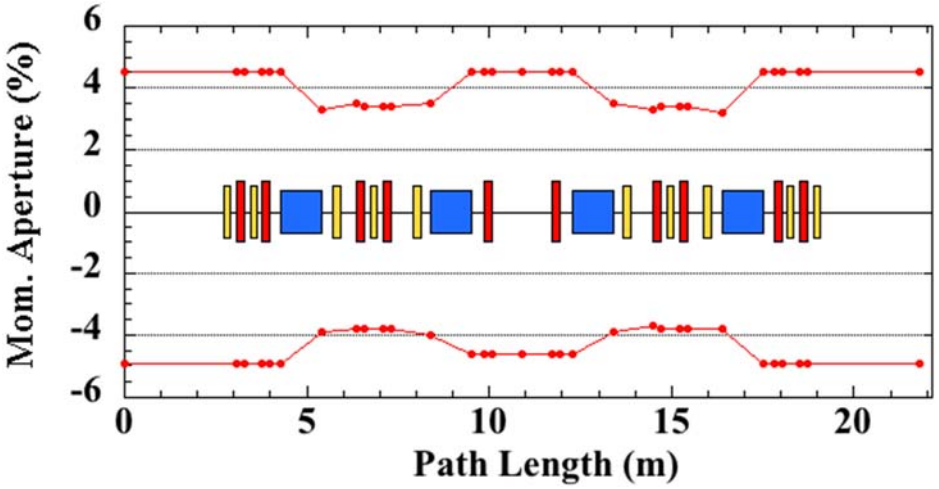

Figure 1.5 Momentum aperture distribution in a cell.

Touschek lifetime was evaluated by numerical calculations with the MA distribution shown in Figure 1.5 and the lattice functions distributed along the ring. The following conditions were assumed: (1) an RF accelerating voltage is 3.6 MV; (2) radiation loss from the bending magnets is only taken into consideration; (3) the smallest aperture among MA, physical aperture, and bucket height determines the beam loss; and (4) electron beam density is adjusted changing the coupling ratio and bunch length. Figure 1.6 shows the dependence of Touschek lifetime on the bunch current. The

calculation was performed for four different conditions combining two coupling ratios with two bunch lengths. Coupling ratios of 0.2% and 1% are a normal value and enhanced one by a coupling control, respectively. Two bunch lengths are a minimum length at a zero current (zero current limit) and longer bunch length at a normal operation current (twice as long as the zero current limit).

Assuming that the target beam current, 400 mA, is stored in about two-thirds of the 592 buckets, the averaged bunch current is 1 mA (a charge of 1.16 nC). In this condition, it is clear that the coupling needs to be increased to approximately 1% to keep a beam lifetime of 5-10 h, which is a rough target value. The bunch length, on the other hand, is longer than the zero current limit due to the effects of ring impedance, particularly potential well distortion. By combining this fact with the effect of the coupling increase, the beam lifetime is expected to be at around 10 h with a stored current of 400 mA and a bunch current of 1 mA.

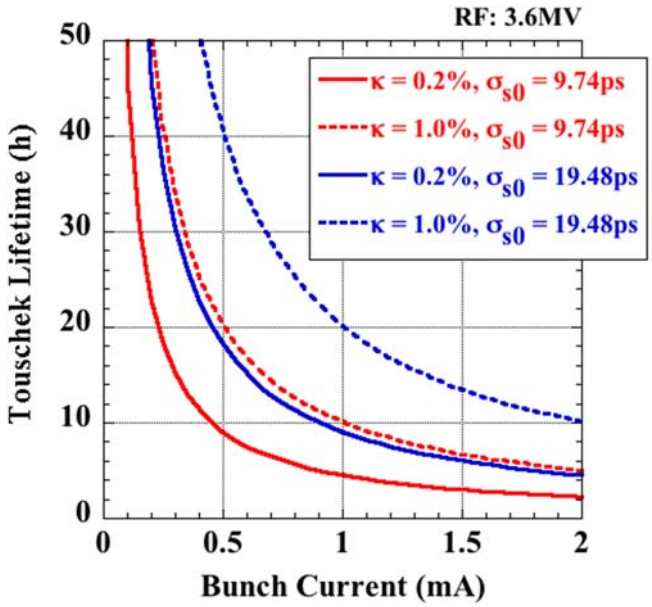

Figure 1.6 Dependence of Touschek lifetime of beam on bunch current calculated using bunch length and coupling as parameters.

Intra-beam scattering (IBS) in the bunch increases beam emittance in the three axial directions. This effect is caused by a small angle scattering, of which energy transfer is too small to cause beam losses. By taking small angle scatterings into account, a dynamic equilibrium where the emittance excitation including the scattering contribution balances radiation damping in the three axes, namely

horizontal, vertical, and energy axes, can be numerically calculated in a self-consistent manner [1.1].

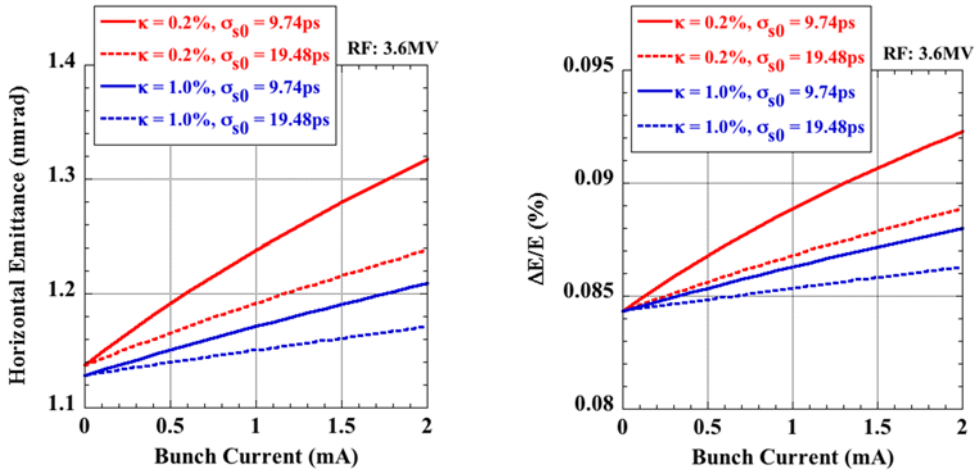

Figure 1.7 Bunch current dependent degradation in horizontal emittance (left) and energy spread (right) caused by IBS.

Figure 1.7 shows increases in the horizontal emittance and energy spread as a function of bunch current. The same calculation conditions were used as those for the numerical calculation of the Touschek lifetime. These results show that the increases in both the horizontal emittance and energy spread are at negligible levels with a coupling ratio of 1% and a bunch current of 1 mA. This condition gives a Touschek lifetime of approximately 10 h.

Reference

[1.1] K.L.F. Bane et al., PRST-AB 5, 084403 (2002).

2. Magnet system

2.1 Magnet

Figure 2.1 shows a magnet configuration in a unit cell. The storage ring consists of 16 unit cells, each of which has four BQ combined, ten quadrupole, and ten sextupole magnets that fold back at the short straight section (indicated as “SS” in the figure) at the center of the cell. The BQ combined magnets provide bending and defocusing functions in a single magnet. Thus, there are a total of one type of BQ combined, five types of quadrupoles, and five types of sextupole magnets. Each type of quadrupole and sextupole magnets are powered in series by a common power supply as a family, while all the BQ combined magnets from a single family powered by a single power supply. A variation of the integrated magnetic fields of magnets in each family needs to be controlled within ±0.2 % for the BQ combined magnets and ± 0.4 % for the quadrupole and sextupole magnets. All the magnets are electromagnets, and all the coils for the magnets are hollow conductor types. To accommodate to the high packing factor lattice, the magnets need to be designed as short as possible by carefully designing compact coil configurations. Another important criterion is power consumption. For that, and also for suppressing thermal deformations of magnets, we set the limit of the current density in the coils below 3.2 A/mm^2. The temperature rise of cooling water under a pressure drop of 0.6 MPa should be less than 5 K to suppress deformation of the magnets.

Measurements of integrated magnetic fields, excitation curves, and field harmonics will be carried out for all the magnets. The excitation curves and flux density distributions in the transverse and longitudinal directions will be measured by a Hall probe, and the field harmonics will be resolved by making use of so-called the single stretched wire (SSW). In the SSW setup, a single wire is rotating or moving according to some rule inside a magnet so that the field harmonics can be analyzed for verifying the field quality of the magnet.

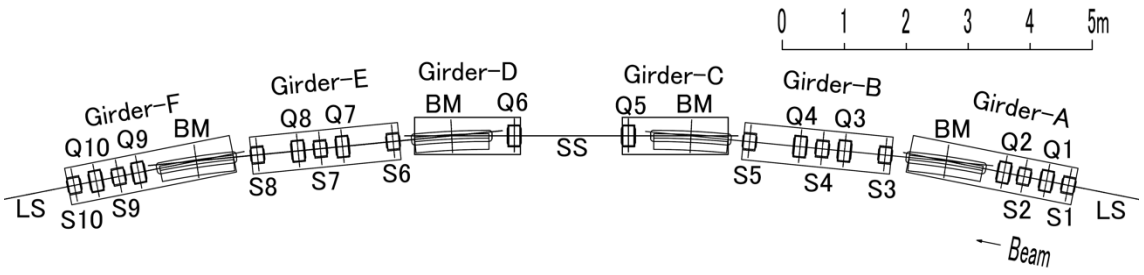

Figure 2.1 Configuration of magnets in a unit cell.

2.1.1 Quadrupole magnets

Specifications of the quadrupole magnets are described in Table 2.1 The core is made with laminated silicon sheets with a thickness of 0.5 mm. The bore diameter is 34 mm and the maximum excitation current is 352 A, which results in the maximum magnetic field gradient of 53 T/m. The effective magnetic length is all 200 mm. For a beam-based alignment and a local correction of the lattice, an auxiliary power supply is connected to an individual quadrupole magnet so that we can independently and finely adjust the magnetic field of each magnet in the same family.

Table 2.1 Specifications of quadrupole magnets.

	Q1	Q2	Q3	Q4	Q5
Bore diameter [mm]	34				
Maximum excitation current [A]	352				
Number of turns in a pole [T/Pole]	17	12	20	20	20
Effective magnetic length [mm]	200				
Total length of magnet [mm]	≤248	≤230	≤248	≤248	≤266
Homogeneity of field gradient [%] (x≤±8 mm)	≤ ±0.1				
Number of magnets	32	32	32	32	32

2.1.2 Sextupole magnets

Specifications of the sextupole magnets are described in Table 2.2. The core is the laminated silicon sheets with the same thickness as quadrupoles, i.e., 0.5 mm, but the bore diameter is 40 mm with a maximum excitation current of 250 A. It corresponds to the field gradient of 2120 T/m^2. The effective magnetic length is all 200 mm. The sextupole magnets are equipped with auxiliary air-cooling coils as it can work as a steering magnet as well. The auxiliary coils are also used for independent tuning of the sextupole field in case of the beam-based alignment. For the purposes, all the three pairs of coils, each of which are connected to a facing pair of poles, can be tuned independently.

Table 2.2 Specifications of sextupole magnets.

	S1	S2	S3	S4	S5
Bore diameter [mm]	40				
Maximum excitation current [A]	250				
Number of turns in a pole [T/Pole]	9	9	9	5	9

Effective magnetic length [mm]	200				
Total length of magnet [mm]	≤259	≤259	≤259	≤309	≤259
Homogeneity of Field gradient [%] (x≤±6 mm)	≤ ±0.1				
Maximum excitation current for auxiliary coil [A]	20				
Number of turns in a pole for auxiliary coil [T/Pole]	48	48	48	20	48
Number of magnets	32	32	32	32	32

2.1.3 BQ combined magnets

Specifications of the BQ combined magnets are shown in Table 2.3. The cross-sectional shape of the pole comes in a truncated hyperbolic curve. A gap length of the magnetic poles is 28 mm along the beam trajectory. We set the maximum excitation current at 650 A for generating a bending field of 0.9 T and a quadrupole field of -7.3 T/m. The effective magnetic length is 1130 mm.

Table 2.3 Specifications of BQ combined magnets.

Gap length along the beam trajectory [mm]	28
Maximum excitation current [A]	650
Number of turns in a pole [T/pole]	16
Effective magnetic length [mm]	1130
Total length of magnet [mm]	≤ 1315
Number of magnets	64

2.1.4 Steering magnets

Six sextupole magnets, i.e., S1, S3, S5, S6, S8, S10, in each cell are equipped with auxiliary coils for steering functions. All the six magnets can provide both horizontal and vertical kicks with the kick angle of up to 0.4 mrad. Besides, a pair of independent steering magnets with the maximum kick angle of 0.3 mrad in both horizontal and vertical planes will be placed at both ends of a multi-pole wiggler (MPW) in the short straight section. Also, another pair of independent steering magnets will be prepared at both ends of an undulator in the long straight section as well.

2.1.5 Girders

There are six common girders in each cell as shown in Figure 2.1. The common girders are labeled A to F from the upstream to the downstream in each cell. Due to the line symmetry of the magnet configuration in the cell, the common girders are also symmetric in such a way that the girder A and F, that B and E, and C and D have the same structure with the opposite direction. Each girder is supported at four positions on a floor, aiming at the suppression of the girder deformation in a long time as well as the easy height adjustment. The girders are designed to keep the deformation due to the magnet weights less than 0.05 mm and the eigenfrequency of the girder vibration larger than 110 Hz. Portions of the accelerator hall floor supporting the common girders are coated by epoxy resin to readily secure the surface flatness and to mitigate the vibration transfer from the floor to the girders.

2.2. Power supplies

The specifications for power supplies are summarized in Table 2.4. These power supplies are controlled by taking advantage of digital feedback control based on an FPGA (Field Programmable Gate Array). In order to suppress the quantum noises in analog-digital conversion, the power supplies have the DCCT-ADC circuits with 24-bit high-resolution converters. There are 11 power supply families for main magnets; one for BQ combined, five for quadrupole, and five for sextupole magnets. In order to reduce development efforts and costs, these power supplies are designed to share most specifications. As a result, there are only two types of quadrupole and one type of sextupole power supplies in addition to BQ combined power supply. These main power supplies for the BQ combined, quadrupole, and sextupole magnets are required to stabilize the ripple and long-term drift of the current within 20 ppm (peak-to-peak). The current control utilizes the chopper-switching scheme based on the PWM (Pulse Width Modulation), of which conversion efficiency is larger than 0.85. Every type of power supply has one backup for a quick replacement in case of the power supply failure.

The independent steering magnets at short straight sections and the ones combined with the sextupoles are driven by the same type of switching power supply, and those at long straight sections are driven by smaller ones as shown in Table 2.4. These are bipolar power supplies that utilize full-bridge switching with the current stability of better than 50 ppm including ripples and long-term drift. We need to synchronize the three power supplies for each pair of steering coils equipped in the sextupole for applying it to the beam-based alignment and other purposes.

Electromagnetic interference between power supplies via magnet poles should also be considered in the design. Auxiliary power supplies connected to individual quadrupole magnets are bipolar type both in current and voltage. The required stability should be better than 50 ppm including ripples and long-term drift.

We run power cables for the family magnets clockwise along the ring and run them back counter clockwise for avoiding to make a current loop along the ring.

Table 2.4 Specifications of electric power supplies

Type	Load	Output	Maximum Current	Maximum Voltage	Ripple Drift	Quantity
BQ combined	BQ	Unipolar	650 A	400 V	20 ppm 20 ppm/8 h	1
Quadrupole Type1	Q1, Q3, Q5	Unipolar	350 A	200 V	20 ppm 20 ppm/8 h	3
Quadrupole Type2	Q2, Q4	Unipolar	50 A	50 V	50 ppm 50 ppm/8 h	2
Sextupole	S1 – S5	Unipolar	250 A	110 V	20 ppm 20 ppm/8 h	5
Steering	Sext. mag. Mag at SSS	Bipolar	±16 A	±8 V	50 ppm 50 ppm/8 h	384
Steering	Mag at LSS	Bipolar	±5 A	±4 V	50 ppm 50 ppm/8 h	96
Auxiliary	Quadrupole	Bipolar	±18 A	±10 V	50 ppm 50 ppm/8 h	96

2.3 Alignment

The alignment procedure is classified into two stages. One is to align magnets in the straight section between BQ combined magnets, and another is to do the alignment between the straight sections. Alignment tolerances for the two stages are listed in Table 2.5.

2.3.1 Alignment in straight sections

At the first step of alignment, magnets are aligned on a common girder on the straight. As is shown in Table 2.5, the tolerance is ±0.05 mm, but we aim to achieve even smaller alignment errors for obtaining adequate dynamic aperture. For the purpose, we apply the vibrating wire technique that we assume is effective to a

precise magnet alignment on the straight. In the scheme, a tensioned wire, excited with an AC current, is placed along the longitudinal axis in a series of magnets and each magnet is powered one by one. Then the field profile of the magnet near its magnetic center is measured by detecting the wire vibration at its resonance frequency. Thus we can directly determine the magnetic centers and do the alignment on the straight without relying on any fiducials [2.1]. On girders A, B, E, and F, magnets are subject to this alignment scheme except for the BQ combined magnets, while on girders C and D, where we only have a BQ combined and a single quadrupole magnet, magnets are aligned based on the conventional laser tracker measurement. Once the magnets are aligned on the straight, we set fiducial points on the magnets at both ends of the straight for preparing for the alignment between the straights. There is one more procedure before proceeding to the alignment between the straights. The magnets on the common girder need to be moved into the accelerator tunnel after finishing the magnet alignment in a straight section. Before moving, we measure with high precision each magnet position by using a newly developed system, called "Wire Alignment Monitoring System (WAMS)". Here, we set a wire position sensor on the SMR (Spherically Mounted Retroreflector) target pedestal on the top of each magnet, and run another wire along with them. We then record the relative magnet positions deduced from the wire positions measured at each wire position sensor. The WAMS is useful when (i) a drift of magnet position upon the move needs to be identified, and (ii) a precise magnet position measurement is necessary with a vacuum chamber already sitting in the magnet. This monitor is expected to give us information on a long-term drift of the magnet position due to the deformation of the girder and others in years.

Table 2.5 Alignment tolerances.

	x, y	Yaw, Pitch, Roll
On straight	±0.05 mm	±0.1 mrad
Between straights	±0.09 mm	±0.1 mrad

The next step is to do the alignment between the straights after moving the magnets aligned on the girder into the accelerator tunnel. Inside the tunnel, girders are aligned using a laser tracker and an alignment level tool. Important criteria for this step are to keep the relative position between adjacent girders within the tolerance (see Table 2.5). Beyond the wavelength of betatron oscillation of electrons, the alignment requirement between girders is rather relaxed. Only we have to do is

to smoothly align girders without a sudden jump of the girder position within the betatron oscillation wavelength. The alignment tolerance for girders is not extremely challenging, so it can be achieved by rather conventional ways based on the network measurement by the laser tracker.

In addition to the above alignment steps, there are other critical issues that we have to consider in carrying out the precise alignment. The temperature drift of ambient air may affect the precision of the alignment. Magnets need to be disassembled by half when the vacuum chambers are installed into the magnets, where the precision of physical repeatability of the magnet yokes may distort the precise alignment. Most of the effects can be monitored by using the WAMS system, but still the careful treatment is the key to reliable alignment works.

Reference

[2.1] K. Fukami et al., “Performance verification of a precise vibrating-wire magnet alignment technique for next-generation light sources”, Rev. Sci. Instrum. 90, 054703 (2019).

3. Vacuum system

3.1 Outline of vacuum system

The vacuum system was designed targeting 20 h of the gas scattering lifetime at a stored electron beam current of 400 mA, which required the pressure of 1×10^{-7} Pa equivalent to CO. Figure 3.1 shows the layout of magnets, vacuum chambers, and photon absorbers for a unit cell. The vacuum system of each cell (unit cell) consists of six straight section chambers and four bending section chambers. The long straight section, where an insertion device (ID) is installed, can be isolated from the straight section 5 (the previous cell) and the straight section 1 by sector gate valve 2 (SGV 2) and sector gate valve 1 (SGV 1), respectively. An ID-dummy chamber is inserted into the long straight section until an ID is installed. In addition, a chamber for a multi-pole wiggler (MPW) is inserted into the center of the straight section 3 (the short straight section). For the material of the vacuum chamber, stainless steel was chosen. Stainless steel CF flanges connect the vacuum chambers.

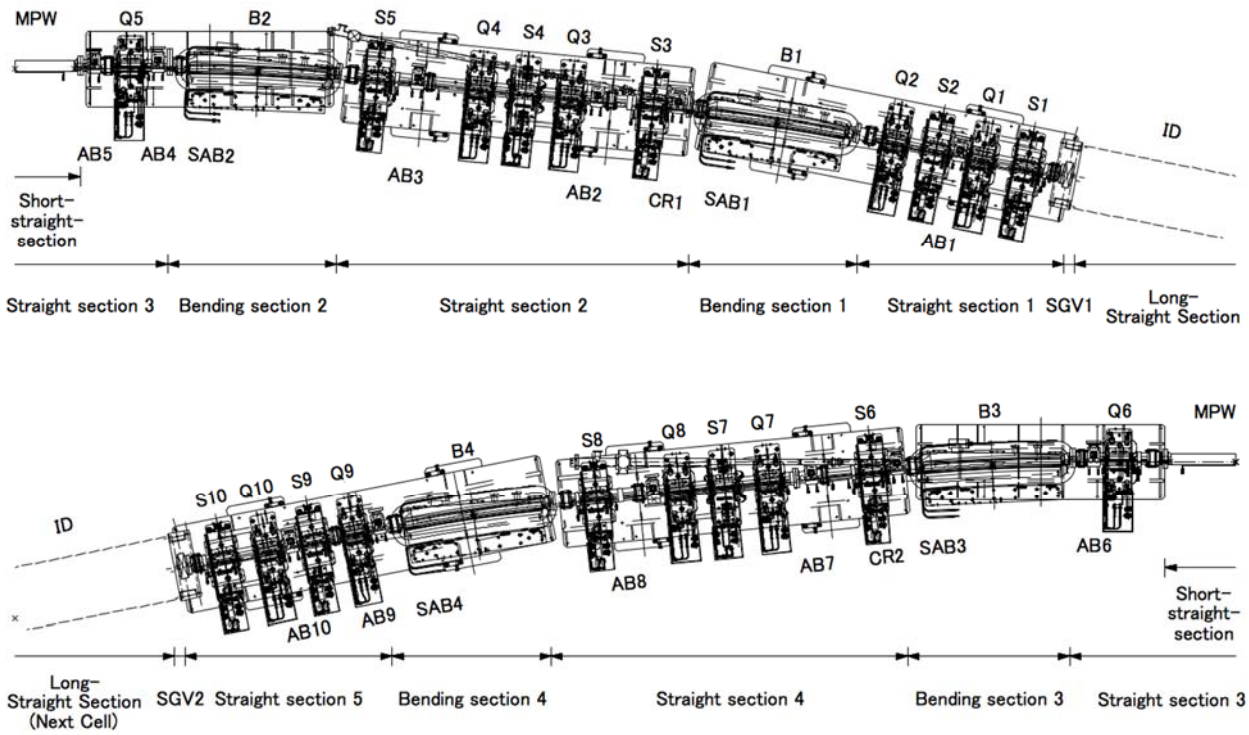

Figure 3.1 Layout of magnets, vacuum chambers and photon absorbers for a unit cell. Bending magnet (B), quadrupole magnet (Q), sextupole magnet (S), photon absorber (CR1, 2, AB1 to 10, and SAB1 to 4).

The 12 photon absorbers (CR1, 2 and AB1 to 10) and four supplemental photon absorbers (SAB 1 to 4) are discretely arranged so that the synchrotron radiation from the bending magnets may not irradiate the chamber wall. By concentrating the vacuum pumps at the photon absorbers, photon stimulated desorption (PSD) gas will be locally evacuated to maintain low pressure even during the beam operations. To protect the stainless steel walls of the vacuum chambers from the collision of the electron beam on the occasion of beam dumps, the AB8 chamber in each cell is equipped with an electron beam absorber made of graphite to spread and absorb the dumped electron beam.

In-situ baking of the vacuum chamber and non-evaporable getter pump (NEG) activation is carried out after installation in the ring tunnel.

3.2 Structure and function of vacuum system

3.2.1 Straight section chamber

Figure 3.2 shows the cross-section of the straight section chamber. The chamber consists of a beam chamber, an antechamber, and a slot that connects both chambers. The height of the beam chamber is set at 16 mm by considering the vertical size of the stored electron beam and the area where the dynamical stability of the electron beam can be secured. The width is set at ±15 mm to secure enough margins for the injection beam orbit. The 5 mm height slot enables the passage of synchrotron radiation from the bending magnets. The inner wall of the antechamber is set at 73 mm from the beam center in the horizontal direction. The discrete photon absorbers are located to prevent the irradiation of synchrotron radiation from the bending magnets to the inner wall of the antechamber.

The chamber is made of stainless steel, which has excellent corrosion resistance and high nonmagnetic stability. The inner top and bottom surfaces of the beam chamber are plated with copper more than 0.1 mm thick to reduce resistive-wall impedance. The vacuum chamber has cooling channels for stabilizing chamber temperature.

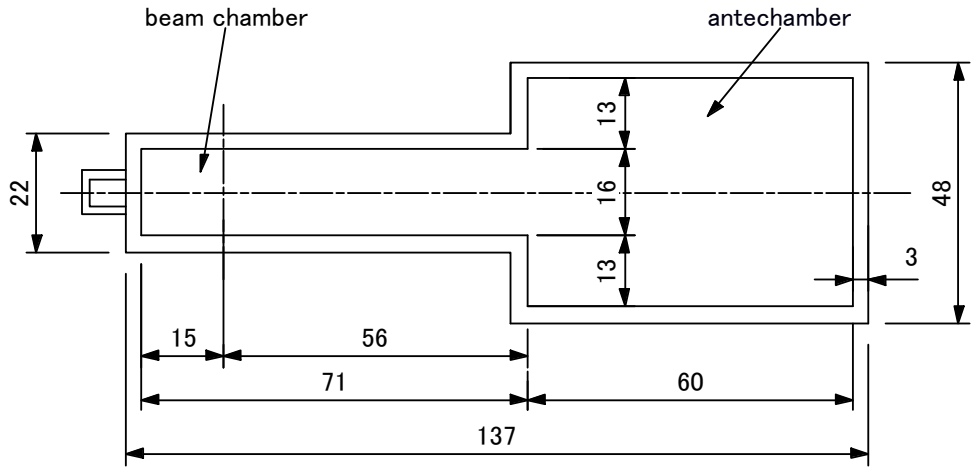

Figure 3.2 Cross-section of straight section chamber. The unit is mm.

3.2.2 Bending section chamber

Figure 3.3 shows the cross-section of the bending section chamber downstream part. The bending section chamber consists of a beam chamber and an antechamber equipped with a supplemental photon absorber at the most downstream. The internal dimension of the chamber is determined to fit in a narrow gap of the bending magnet poles without significant cross section deformation at atmospheric pressure and to extract all ±4.0 mrad synchrotron radiation from the MPW. The chamber is also made of stainless steel. The stainless steel plates formed by bending are cut in accordance with the bending radius, and connected by laser beam welding (LBW) to build the chamber. The inner top and bottom surfaces of the beam chamber are also plated with copper more than 0.1 mm thick to reduce resistive-wall impedance.

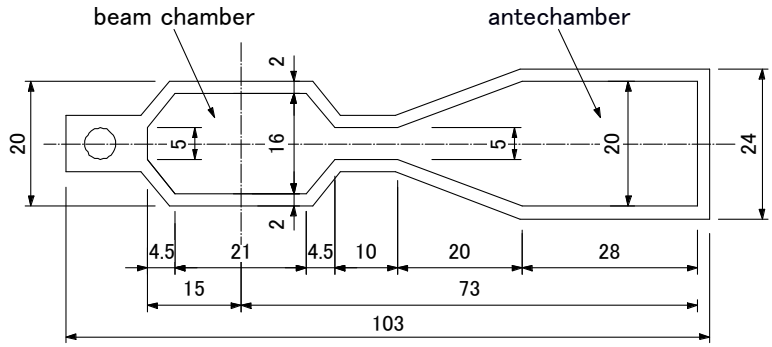

Figure 3.3 Cross-section of the bending section chamber downstream part. The unit is mm.

3.2.3 Photon absorber

The photon absorbers should be positioned properly with an appropriate light cut position in the horizontal direction, taking into account the need to prevent the unwanted radiation to the vacuum chamber walls, to prevent the radiation power allocated to each photon absorber from being excessively large, and to extract the light with a required divergence angle to the beamline (see Figure 3.1). The unit cell has two crotch absorbers (CRs), ten absorbers (ABs) and four supplemental photon absorbers (SABs). The difference between a CR and an AB is the presence or absence of a window for extracting the light to the beamline. The CRs and ABs with proper cooling ability are supposed to be attached to dedicated chambers by flange interface with no gap, which intends to accurately position the irradiation body. The CRs and ABs have structures for confining scattered radiation in the absorber as much as possible. CR1 and CR2 located at the downstream of the ID and the MPW have windows for extracting light with a horizontal divergence angle of ±1.5 mrad and ±4.0 mrad, respectively. SAB is located at the most downstream of the bending section chamber.

Table 3.1 shows a list of power distribution on each photon absorber at the stored beam current of 400 mA. The CRs and ABs are designed based on the results of thermal and thermomechanical analyses and are made of GLIDCOP that has high mechanical strength at higher temperatures [3.1]. The heat-absorbing part is designed with simple grazing angle configuration to have a peak power density of about 200 W/mm^2 (normal incidence equivalent). The SABs are made of oxygen-free copper (OFC) because the maximum temperature and equivalent stress do not exceed 200°C and the yield point. In the design of the cooling mechanism, it is crucial to not only incorporate flow passage structure adaptable to miniaturization but also prevent the corrosion of the heat-absorbing part [3.2] caused by the interaction between the cooling water and synchrotron radiation. In addition, it is also important to keep the flow rate as low as possible to prevent a vibration problem.

Table 3.1 List of absorbed total power (TP) on each photon absorber with peak power density (PPD) at normal incidence.

	CR1	AB2	AB3	SAB2	AB4	AB5	AB6	SAB3
TP (kW)	1.80	1.44	0.40	0.24	1.81	1.33	0.53	0.15
PPD (W/mm^2)	210.9	131.5	26.7	8.8	210.9	163.3	23.0	10.0

	CR2	AB7	AB8	SAB4	AB9	AB10	(IDD _ ab)	AB1	SAB1	Total
TP (kW)	1.77	1.54	0.38	0.26	1.71	1.55	0.38	0.20	0.04	15.53
PPD (W/mm^2)	215.9	131.5	30.7	8.8	215.9	126.6	27.6	2.6	1.6	—

3.2.4 Vacuum chamber parts

CF flanges made of stainless steel connect the vacuum chambers. Beryllium copper RF contacts are inserted to fill the gap between the flanges.

Two types of welded stainless-steel-bellows are designed to efficiently fit in the narrow space between multi-pole magnets. The short-stroke bellows absorbs the misalignment of the chambers. The long-stroke bellows is retracted when the vacuum chamber is inserted in the storage ring, or absorbs thermal expansion of the chambers during baking. Inside the bellows, RF shield made of Beryllium copper is installed to maintain the RF continuity between adjacent chambers. Due to the severe packing factor, it is important to make bellows parts as small as possible. In addition, there is a need to suppress the increase in impedance carefully taking into account the small cross-sectional dimensions of the beam chamber. In order to connect the cross-sections of the vacuum chamber and parts continuously, steps and gaps of the cross-sections must be minimized.

All-metal sector gate valves with RF shields are installed on each side of an ID vacuum chamber to facilitate vacuum maintenance when the chamber is vented to atmospheric pressure. If the pressure deteriorates in any section, these sector gate valves are closed and the section is isolated.

The pressure is monitored by cold cathode gauges, which do not require maintenance because there is no filament to burn out. Signals from the cold cathode gauges and ion pumps are used for the interlock closing the sector gate valves.

3.2.5 Pumping system

In the 3-GeV storage ring, since most of the synchrotron radiation from the bending magnets is received by photon absorbers, outgas due to PSD is localized around the photon absorbers. As a small cross-sectional area of the vacuum chamber makes it difficult to ensure sufficient conductance in the longitudinal direction, a lumped pumping system comprised of a cartridge NEG pump and ion pump is installed near the photon absorbers. The effective pumping speed required for the pumping system is about $0.1 m^3/s$ for CO.

3.3 Gas scattering lifetime and pressure

3.3.1 Gas scattering lifetime

The lifetime of the stored electron beam is mainly determined by the quantum lifetime resulted from the emission of synchrotron radiation, Touschek lifetime decided by Intra-beam scattering inside the bunch, and the gas scattering lifetime caused by the collision with residual gas. Taking into account the RF voltage of 3 MV, the quantum lifetime is adequately long. However, the Touschek lifetime is about 15 h. To prevent the gas scattering lifetime from having significant effects on the beam lifetime, it is required to ensure the gas scattering lifetime of approximately 20 h at the stored beam current of 400 mA. Considering the minimum gap of the insertion device and optical lattice function in the vertical direction, the required ultimate pressure is estimated to be approximately 1×10^{-7} Pa (converted to CO pressure).

3.3.2 Amount of outgassing

The outgassing in the vacuum system of a dedicated light source storage ring is caused by thermal desorption and PSD. In the pressure distribution calculation shown below, the thermal desorption yields of H_2 and CO of stainless steel were set to 2.8×10^{-9} and 7×10^{-10} $Pa \cdot m^3 / s / m^2$, respectively, and the outgassing was allocated according to the surface area of the vacuum chamber. The outgassing due to the PSD was allocated to each photon absorber according to the number of photons and the number of integrated photons, based on the parameter [3.3] used in the vacuum system design at SPring-8-II.

3.3.3 Pressure distribution

Figure 3.4 shows the calculated vacuum pressure distribution in a unit cell at 400 mA operation after 1500 Ah conditioning. In the figure, S = 0 is the position of the sector gate valve 1 at the downstream end of the ID section. An ID-dummy chamber is inserted in the ID section. As a result of the calculation, the average pressure of CO was 6×10^{-8} Pa, the gas scattering lifetime was about 22 hours, and the beam lifetime was 9 hours.

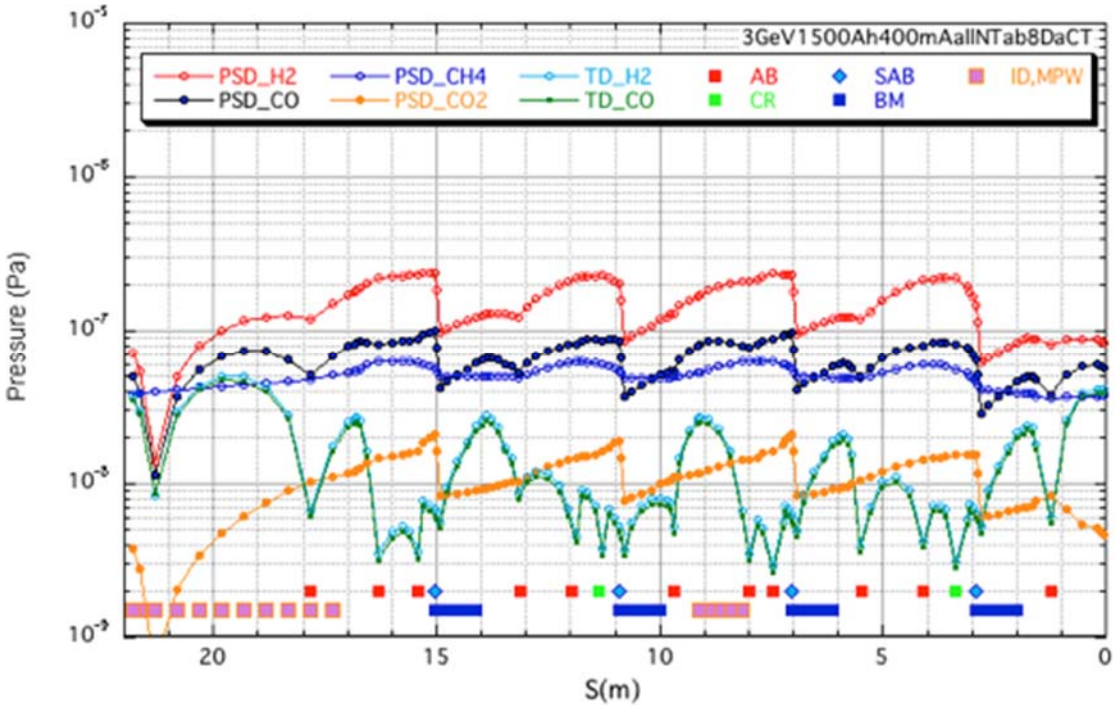

Figure 3.4 Calculated vacuum pressure profile in a unit cell at 400 mA after 1500 Ah conditioning.

References

[3.1] S. Takahashi, et al., J. Synchrotron Rad. 15, 144 (2008).

[3.2] M. Shoji, et al., Vacuum 84, 738 (2010).

[3.3] M. Oishi, et al., Proc. of IPAC2016 THPMY001, Busan, Korea, 3651 (2016).

4. RF acceleration system

4.1 Overview

The role of the RF acceleration system in the storage ring is to compensate for the energy loss of the electron beam due to the generation of synchrotron radiation (radiation loss) at the bending magnets and the insertion devices. This radiation loss is estimated to be up to 1.26 MeV per turn. An RF power of approximately 1 MW must be continuously supplied to the RF cavities to compensate for the radiation loss at a beam current of 400 mA and to generate an acceleration voltage of more than 3.6 MV ensuring a beam lifetime of more than 5 hours. About 500 kW of RF power is consumed over the walls in the RF cavities. To supply such high power with high stability, we will build an acceleration system using the 500 MHz band RF acceleration technology. This frequency band is selected because many pieces of RF equipment have been developed in this band and utilized for accelerators for high-energy physics experiments and synchrotron radiation sources [4.1][4.2]. The equipment has high stability, high power-efficiency, and is relatively inexpensive.

When a high current beam passes through a cavity, parasitic higher-order modes (HOMs) of the cavity are strongly excited. The HOMs are harmful because they force the beam to start unstable motion. This instability is called coupled-bunch instability (CBI). It degrades the emittance and finally leads to beam loss. A TM020-mode RF accelerating cavity with built-in HOM absorbers [4.3][4.4] was designed to damp the HOMs and to suppress the CBIs. The cavity can generate high accelerating electric fields required for high current beam acceleration efficiently.

Table 4.1 and Figure 4.1 show the design parameters and the configuration of the RF acceleration system. The acceleration system consists of (1) an RF source including its driving power supply and a power-transmission system, (2) four acceleration cavities, and (3) a low-level RF control system, each of which is described in the following sections.

Table 4.1 Specification of the storage ring RF acceleration system

Items	Specification
Beam energy	3 GeV
Beam current	400 mA
Beam revolution frequency	859.4 kHz
RF frequency	508.759 MHz
Energy loss	1.26 MeV/turn max.
Bending magnet	0.62 MeV/turn
Insertion device	0.64 MeV/turn max.
RF cavity voltage	3.6 MV (900 kV per cavity)
Synchronous phase	160 - 170° (depends on energy loss)
Synchrotron frequency	6.0 kHz
Number of RF cavities	4 cavities
Heat dissipation at cavity	119 kW per cavity
Input RF power	245 kW per cavity max.

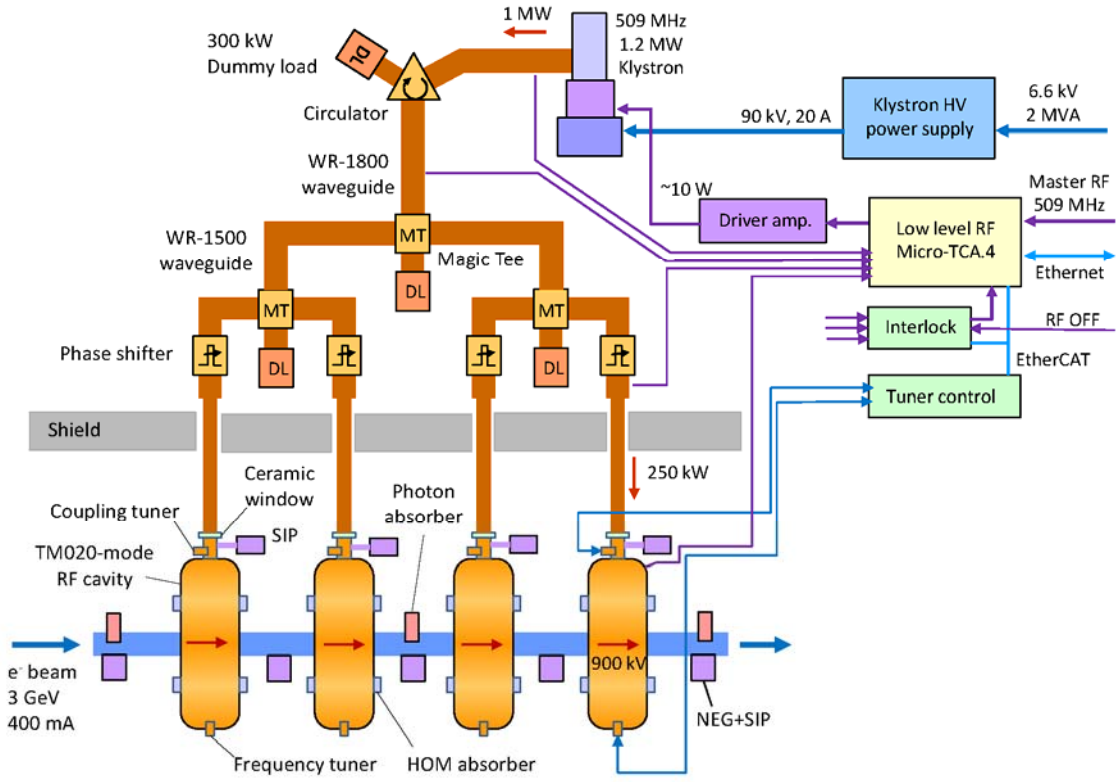

Figure 4.1 Configuration of RF acceleration system

4.2 High-power RF source and transmission system

When RF power exceeds 1 MW, the solid-state amplifier is still too expensive and impractical. Therefore, we adopt a 1.2 MW continuous-wave klystron with a high degree of efficiency [4.5][4.6], which has been used for more than 30 years. This klystron is a triode tube with an anode electrode enabling a high power-efficiency of 60-70% by adjusting its voltage according to the output power. Because a gain of the klystron is over 50 dB, the klystron can provide 1.2 MW power with an input power of approximately 10 W from a driver amplifier. The klystron output power is controlled by the input power and the anode voltage while the cathode voltage is kept at 90 kV. A simple 12-phase full-wave rectifier is used as the power supply to apply a high DC voltage of 90 kV and a current of 20 A in maximum to the cathode of the klystron.

In order to transmit the high-power RF generated by the klystron to the accelerating cavities, a high-power transmission system is constructed using a waveguide of WR-1800 and WR-1500 standards. A circulator [4.7] with a rated forward power of 1.2 MW and a rated reverse power of 650 kW is installed directly downstream of the klystron to protect the klystron from the reflected power. A dummy load with a rated power of 300 kW (maximum allowable power of 3 MW at 20 ms) is connected to the third port of the circulator to absorb the reflected power. After passing through the high-power phase shifters, the RF power flows into the four accelerating cavities. We use special waveguides with cross-sectional dimensions of 381 mm × 100 mm from the through-holes of the storage ring tunnel to the cavities in order to reduce radiation leakage from the holes.

4.3 RF accelerating cavity

We employ the compact TM020-mode RF accelerating cavities developed at SPring-8 to generate a high accelerating voltage, to install four cavities in the 5-m straight section and to suppress the CBI at the high storage current. Figure 4.2 shows a photograph of a prototype of the cavity. The figure also indicates the distributions of the electric and magnetic fields from 3-D RF simulation. The estimated shunt impedance is 6.8 MΩ and the unloaded Q value is 60,300 with the cavity material of oxygen-free copper. The cavity has two slots inside the body along the nodes of the magnetic fields of the TM 020-mode to prevent the TM020-mode from entering the slots. On the other hand, the fields of the HOMs pass through the slot and are attenuated by the ferrite absorbers installed in the slots. Figure 4.3 shows the impedance distributions of the monopole and dipole HOMs obtained from the simulation. Black and red dots indicate the impedances with and without the

absorbers, respectively. The impedance of the beam accelerating mode is not degraded by the absorbers though the HOM impedances can be attenuated to below the CBI thresholds.

For the connection between the cavity and the waveguide, we use a special coupler and adjust the coupling according to the beam loading in high-power operation [4.8]. A variable length copper plunger (coupling tuner) is installed in front of the iris of the cavity, and the coupling value can be varied from 1 to 4 or more by changing the insertion length of the plunger. In this way, the reflected power from the cavity can be reduced and the RF power can be used effectively by keeping the optimum coupling in accordance with the beam current (400 mA max.).

In order to evacuate the cavity and feeding an RF power into the cavity, a ceramic window is installed in the waveguide [4.3]. The window is made from a low-loss alumina-ceramics (dielectric loss < 0.0001), which is bonded to a copper plate with an iris shaped into a racetrack. If damage to the ceramics happens, the window can be easily replaced.

In order to confirm the RF performance of the designed cavity and to conduct high-power RF operation tests, a prototype cavity was fabricated (Figure 4.2). When the cavity has the HOM absorbers made of ferrite, Q-values of major HOMs such as TM110 and TM011 were less than 1,000 sufficient for damping. On the other hand, a decrease in Q-value of the TM020 mode was only 1.4%, as expected. A high-power test was carried out at a test stand of the SPring-8. An RF power of 120 kW was fed into the cavity to generate a voltage of 900 kV for the designed beam acceleration, and there were no serious problems [4.4].

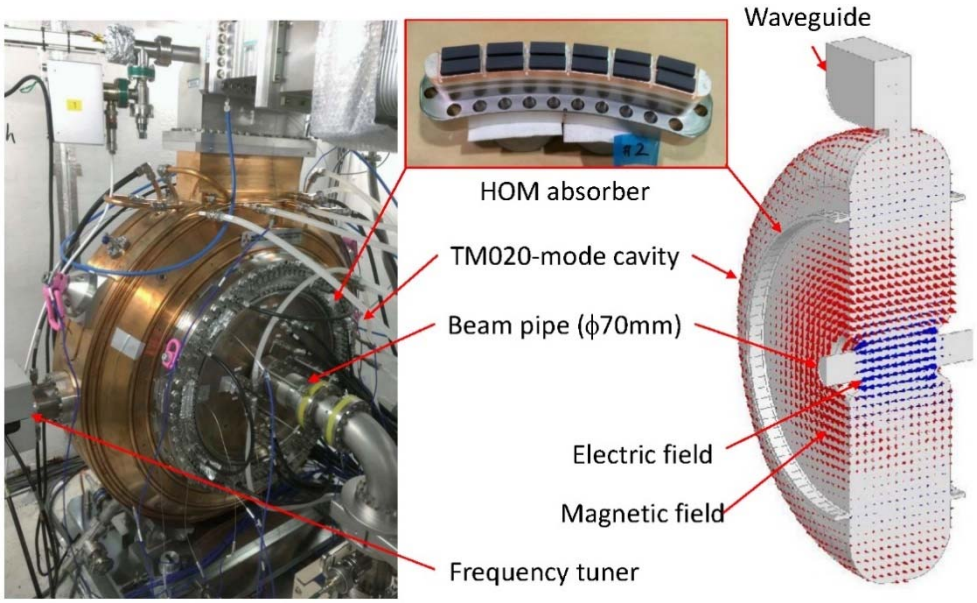

Figure 4.2 Photographs of the TM020-mode RF cavity and the HOM absorber (left), and distribution of electric and magnetic fields by a simulation

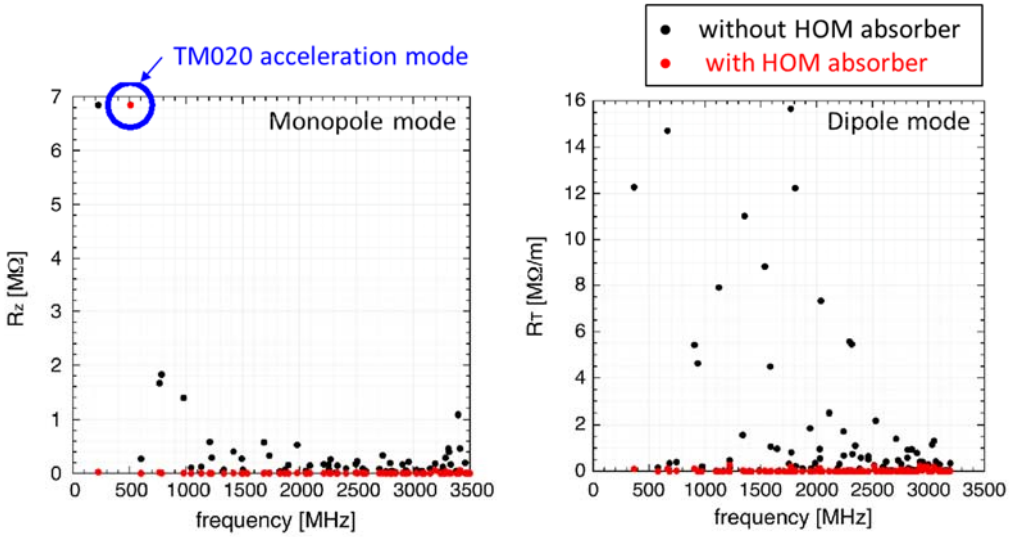

Figure 4.3 Impedance map of monopole mode (left) and dipole mode (right). The blue circle indicates the beam acceleration mode.

4.4 Low-level RF control system

One of the main functions of a low-level RF control system is to stabilize the amplitude and the phase of the acceleration voltage. A digital control system based on the MicroTCA.4 standard [4.9] will be adopted. The merits of this system are to reduce the size and cost of the system by using highly integrated modules and to

improve the control functions. A similar system was introduced in the SPring-8 storage ring in 2017 and has been working stably.

Figure 4.4 shows the configuration of the digital control system. The RF signals from the waveguide or accelerating cavity pickup are fed to a signal processing RTM (Rear Transition Module). The processed signals are fed to a 10-channel digitizer AMC (Advanced Mezzanine Card) capable of sampling at 16 bits and 370 MHz. The Digital Down Conversion is performed by the firmware running on the FPGA in AMC and the amplitude and the phase of the RF signal are obtained. To generate the drive RF signal of the klystron, two channels of DACs on the AMC are used. These signals are fed to the RTM to control the vector modulated RF output. Advanced functions, such as vector summation of the signals from several cavities, RF phase rotation, and numerical operation of feedback control, are realized by the firmware running on the FPGA in AMC.

The acceleration voltage and phase are stabilized by a two-loop feedback controller: the klystron loop and the cavity loop. The klystron loop has a control bandwidth of a few kHz and suppresses the fast output fluctuations caused by the high voltage ripple of the klystron power supply. The cavity loop suppresses slow variations in the order of a few Hz, such as changes in beam load, environmental temperature, and cooling water temperature.

The resonant frequency of the acceleration cavity is adjusted by a motorized plunger (frequency tuner) installed in the cavity. The position of the frequency tuner is controlled so as to keep the phase difference between the input RF signal to the cavity and the pickup RF signal of the cavity constant.

The coupling strength between the waveguide and the cavity is controlled by adjusting the coupling tuner to suppress the power reflection from the cavity since the optimum coupling strength depends on the beam load.

The system also has a function to monitor the operating status of RF devices and abnormal conditions, such as arcing at the ceramics windows, high reflection power from cavities, and so on. If the system detects an abnormal event, the RF switch is cut off immediately and the operation of the klystron is stopped to protect the RF equipment.

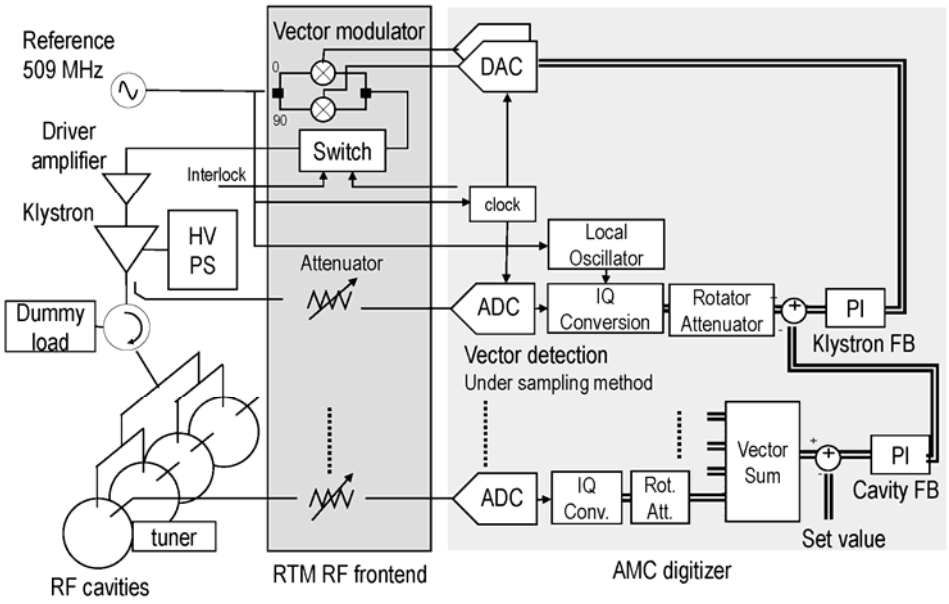

Figure 4.4 Schematic of the digital low-level RF system

References

[4.1] http://www-superkekb.kek.jp//

[4.2] Y. Kawashima et al., Proc. of EPAC08, Genoa, p. 1485 (2008).

[4.3] H. Ego et al., Proc. of 11th PASJ meeting, Aomori Japan, p237 (2014).

[4.4] H. Ego et al., Proc. of 16th PASJ meeting, Kyoto Japan, p17 (2019).

[4.5] S. Isagawa et al., Proc. of PAC87, Washington D.C., p. 1934 (1987).

[4.6] M. Hara et al., J. Synchrotron Rad.5, 379 (1998).

[4.7] H. Ego et al., Proc. of EPAC94, London, p. 1865 (1994).

[4.8] H. Ego, Nucl. Instr. Meth. A564, p. 74 (2006).

[4.9] T. Ohshima et al., Proc. of IPAC17, Copenhagen, p. 3996 (2017).

5. Beam diagnostic system

5.1 Outline of beam diagnostic system

The beam diagnostic system is important to generate high-quality synchrotron radiation by monitoring and controlling the electron beam. This chapter describes the beam diagnostic instruments in the storage ring and the injection beam transport line near the storage ring.

The diagnostic instruments in the beam transport line near the injection point to the storage ring are listed in Table 5.1. To inject the electron beam stably and efficiently with the beam injection system in Chapter 6, both the beam profile and the injection beam orbit have to be adjusted to fit the dynamic aperture of the storage ring. Sufficient clearance between the injected beam and the septum wall and small amplitude betatron oscillation of the injected beam should be realized by adjusting the injection beam orbit and the optics of the beam transport line. We install an OTR-based beam profile monitor to measure the injection beam size and two beam-position monitors (BPMs) to determine the injection beam orbit. We also install a current transformer (CT) to evaluate the beam injection efficiency by comparing the injection beam charge from this CT and the increase in the stored beam current of the ring measured by with a DCCT (described later).

The diagnostic instruments in the storage ring are summarized in Table 5.2. BPMs are installed along the whole storage ring to monitor both the single-pass beam trajectory of the injected beam and the equilibrium orbit of the stored beam. A DCCT is used for the stored beam current measurement and a stripline BPM is employed to monitor the current and the longitudinal phase of each electron bunch and to diagnose the orbit fluctuations etc.

To provide stable x-rays to users, a reliable x-ray beam-position monitor (XBPM) to monitor the optical axis precisely is essential. A conventional blade-type XBPM is not good enough for this purpose since the position reading of this XBPM depends on the gap of the insertion device. The blade-type XBPM detects not the core center of the X-ray beam but just the tail part of the x-ray beam profile that changes with the gap movement of the insertion device. Therefore, we need to develop a new XBPM sensitive to the center of the core of the x-ray beam according to the latest researches for the SPring-8-II, etc.

The beam size at the source point for each beamline is estimated from the emittance and the x-y coupling ratio obtained at one location with the information from the orbit response matrix measurement by the BPMs. The emittance and x-y coupling

ratio are measured by a beam size monitor, which detects the X-ray synchrotron radiation from a 3-pole wiggler.

A real-time betatron tune monitor is also equipped for the evaluation of the beam optics and the automatic compensation of the tune shift due to the gap change of insertion devices. To save the installation space for the instruments and to realize a real-time measurement capability, the tune monitor is implemented in the bunch-by-bunch feedback (BBF) system described later.

The beam diagnostic instruments in the storage ring, except for the BPMs and XBPMs, are installed into two short straight sections dedicated to beam instrumentation.

Table 5.1 Beam diagnostic instruments for the injection beam transport line

Instrument	Number of units
Beam size monitor	1
Beam position monitor (BPM)	2
Beam charge monitor (current transformer, CT)	1

Table 5.2 Beam diagnostic instruments for the storage ring

Instrument	Number of units
Beam position monitor (BPM)	112 (7 per cell)
Stored beam current monitor (DCCT)	1
Stripline BPM	1
Photon beam position monitor	1 per beamline
Beam size monitor	1
Betatron tune monitor	1 (implemented in BBF)
Beam instability control system (BBF)	1

5.2 Beam position monitor

As described in Table 5.2, 7 BPMs are installed in each unit cell. The signal of the beam is picked up by button-type electrodes developed for the SPring-8-II. This electrode was carefully designed to suppress the impedance and heat generation [5.1]. The BPM vacuum chamber (BPM block) is shown in Figure 5.1. The chamber has a bulk stainless steel part to mount button electrodes and a water cooling channel to reduce temperature rise. For the geometry of the BPM block, the beam position sensitivity factor is estimated to be approximately 7 mm for both x and y directions, with which sufficient precision of the beam position can be obtained. The BPM block

has precise fiducial planes on the outer surface to survey the BPM block with respect to adjacent quadrupole and sextupole magnets.

The BPM readout electronics are required to have both the single-pass detection and the equilibrium orbit monitor functions with sufficient precision, accuracy, and stability. The single-pass trajectory data of the injected beam is essential for the beam commissioning of the ring. The precise equilibrium orbit data is crucial for stable user operation. Furthermore, an interlocking logic to abort the beam storage is needed for the BPMs adjacent to the insertion devices in case of an abnormal beam orbit shift since the intense radiation from the insertion devices can damage the vacuum chamber of the storage ring. The transient beam orbit fluctuation measurement function on beam loss events etc. is also demanded. To implement all these functions, the BPM electronics must be operated with several data rates in parallel, such as turn-by-turn, 10 kHz, and 10 Hz. As a sufficient solution, we employ a BPM electronics system based on the MicroTCA.4 standard [5.2], which was developed for the SPring-8-II.

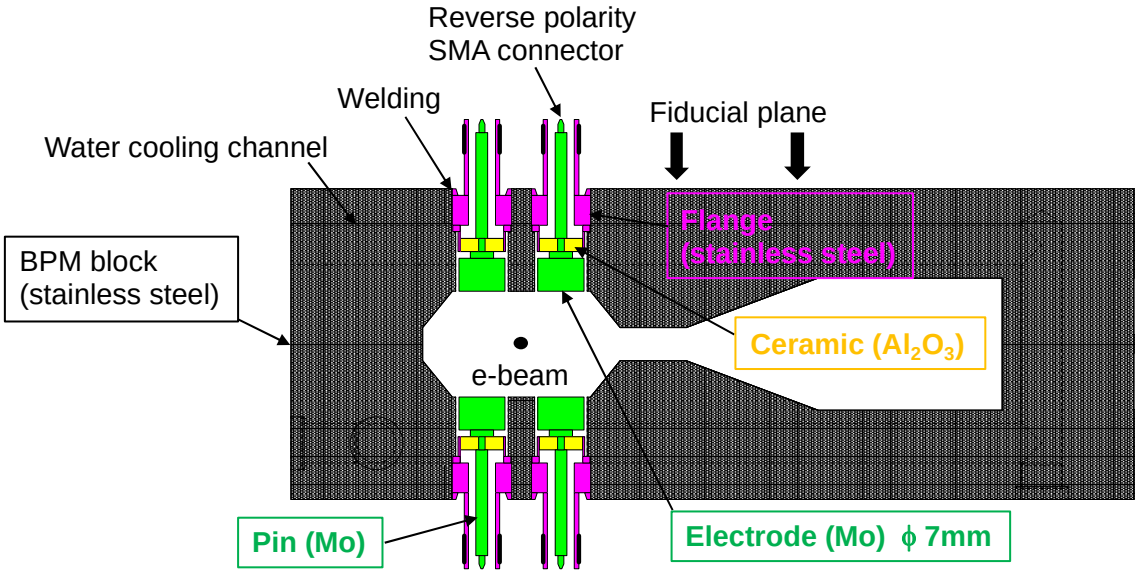

Figure 5.1 Cross-section of the vacuum chamber with BPM electrodes (BPM block).

To deliver stable synchrotron radiation to users, the beam orbit stability is quite important. The BPM block and its girder should be designed to suppress the thermal deformation. The signal cables are required to have low loss, small reflection, and radiation-resistance for long-term stability and good temperature tolerance. The readout electronics are also demanded to be highly stable and the temperature of the electronics should be regulated to reduce the thermal variations.

The calibration procedures of the BPM system before the beam commissioning will be investigated based on the required position accuracy and the commissioning strategy. After the success of beam storage, the BPM offset will be calibrated by using an electron beam (beam-based alignment). The BPM offset with respect to the field center of an adjacent quadrupole or sextupole magnet is demanded to be measured with an accuracy of better than 10 μm.

5.3 Beam size monitor using synchrotron radiation

A 3-pole wiggler is installed to one of the short straight sections of the ring to measure the beam emittance and the x-y coupling ratio. The wiggler radiation is detected by an x-ray pinhole camera, which is designed by improving the one operating at the SPring-8 storage ring [5.3]. The spatial resolution of the pinhole camera is expected to be a few μm. Visible radiation from the 3-pole wiggler is also extracted to evaluate the bunch length, etc. The x-ray pinhole camera is installed inside the storage ring tunnel and the darkroom for the visible light detection is built in the experimental hall.

5.4 Control of beam instability

The suppression of beam instability is necessary to stably circulate the high-current electron beam of 400 mA within the narrow vacuum chamber described in Section 3. Since the storage ring will be operated with the top-up injection, the chromaticity has to be small enough to minimize the loss of the injected beam. Therefore, a bunch-by-bunch feedback (BBF) system to control the beam instability is utilized from the early stage of the operation. The schematic diagram of the BBF system is shown in Figure 5.2. Beam position signals are picked up by stripline electrodes, the counter kick signal is calculated by an FPGA-based electronics, and stripline kickers manipulate the beam orbit. The FPGA-based BBF electronics are widely used in other facilities and the stripline electrodes and the wide-band amplifiers are already developed in SPring-8. The BBF system is designed according to these successful experiences.

As mentioned in Section 5.1, the BBF system is also utilized for the real-time betatron tune monitor.

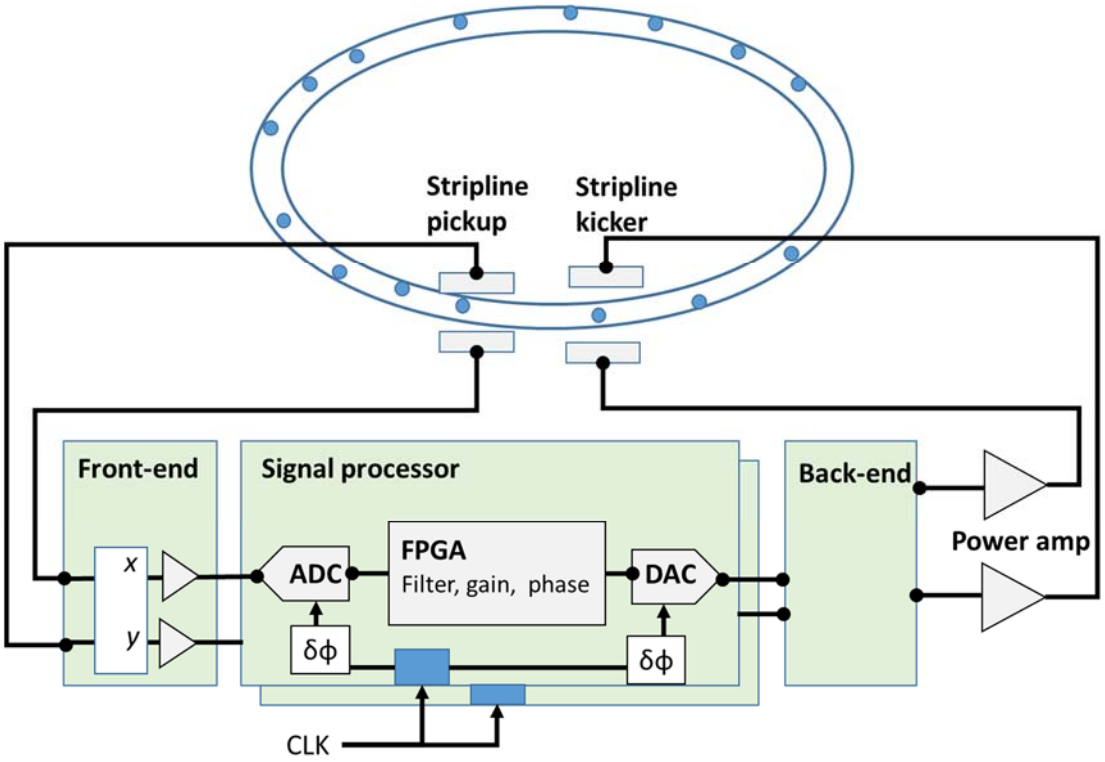

Figure 5.2 Block diagram of the transverse BBF system.

References

[5.1] M. Masaki, et al., Proc. of IBIC16, Barcelona, TUPG18 (2016).

[5.2] H. Maesaka, et al., Proc. of IBIC19, Malmo, WEBO03 (2019).

[5.3] S. Takano, et al., Proc. of IBIC15, Melbourne, TUCLA02 (2015).

6. Beam injection system

6.1 Outline of beam injection system

We adopt an off-axis beam injection system to the storage ring. The high-performance linear accelerator described in Section 7 is used as a full energy injector of low-emittance beams to enable a compact, highly efficient and stable beam injection system. The beams are injected from the inside of the ring to a position shifted horizontally from the stored beam orbit. Septum electromagnets to deflect the injected beam and four kicker magnets for the injection orbit bump are installed in the 5.4m long straight section of the cell 4.

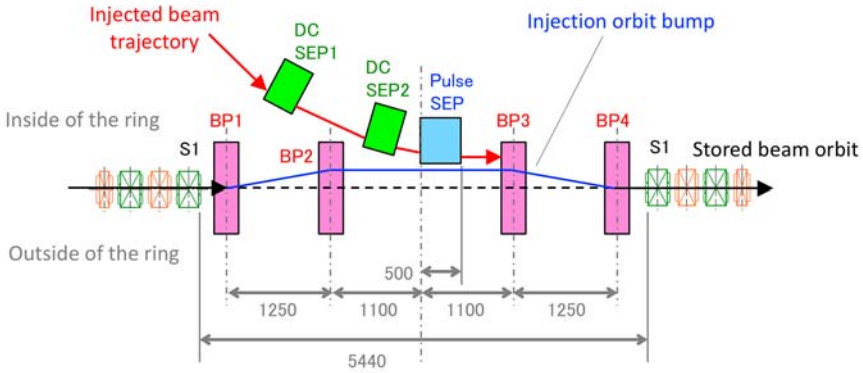

Figure 6.1 Schematic of the beam injection system. Numbers without units in the figure represent millimeters.

Figure 6.1 shows an overview of the beam injection system. The injection system consists of four kicker magnets (BP1 to BP4) and three septum magnets (DC SEP1, DC SEP2, Pulse SEP). A differential pumping system is installed upstream of the septum magnet (DC SEP1) to connect the beam transport vacuum to the ultra-high vacuum of the storage ring without a Be window that deteriorates the emittance of the injected beam. Non-linear magnets such as sextuple magnets are not included inside the injection orbit bump so that the beam fluctuation at the moment of beam injection does not affect the experimental users.

6.2 Parameters for beam injection

The beam parameters at the injection point into the storage ring assumed for the design of the beam injection system are shown in Table 6.1. The positional relationship between the injected beam and the stored beam orbit is illustrated in Figure 6.2. The effective beam size (r.m.s.) of the injected beam and the accumulated

beam at the injection point are 245 μm and 114 μm, respectively. The pulsed septum electromagnet (Pulse SEP) is of in-vacuum type, and the effective thickness of the septum wall, the total thickness of the eddy current shield plate and the magnetic field shield, is 1 mm including the manufacturing accuracy. The orbit bump height required for beam injection depends on the size of the physical aperture at the injection point. The smaller this aperture is, the easier the design of the kicker magnets for the orbit bump. A smaller aperture, on the other hand, means smaller distances from the stationary ring orbit and the bumped orbit, respectively, to the septum wall of the pulsed septum magnet. It could potentially cause the beam instability, the beam loss, and tuning difficulties of the storage ring as well. Here, the distance from the stored beam orbit to the septum wall is set to 8.5 mm, and the height of the pulsed orbit bump to 6 mm. In the startup of the storage ring operation, we assume the position of the injected beam in the range of 2 mm to 4 mm from the septum wall. We would aim to reduce the maximum amplitude of beam injection down to about 6 mm by adjusting the injection beam position as close as 2 mm from the septum wall. When an on-axis beam injection is required for the commissioning of the ring and the beam tuning later on, an auxiliary DC orbit bump should be created with the steering electromagnets on both sides of the beam injection section and superimposed on the pulsed orbit bump generated by the kicker magnets.

Table 6.1 Stored beam and injected beam parameters at the beam injection point

Parameters	Symbol	Injected beam	Stored beam
Horizontal emittance	ε_x	3nm rad	1nm rad
Energy dispersion	σ_E/E	0.1%	0.084 %
Betatron and dispersion functions	β_x、Dx	20m, 0m	13m, 0m
Beam size (σ)	σ_x	245μm	114μm

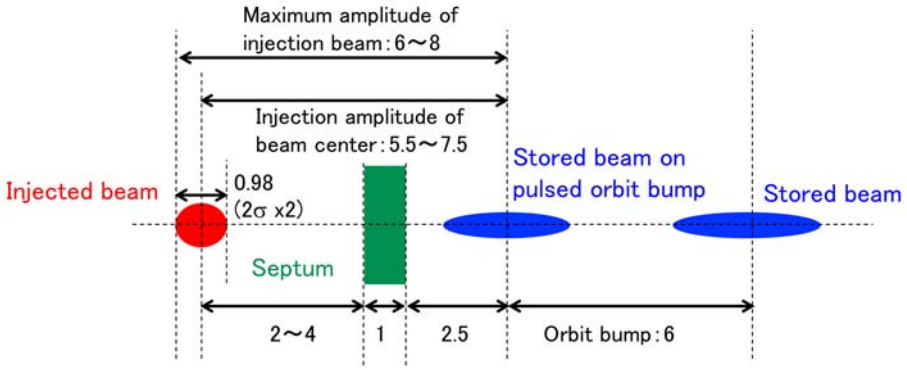

Figure 6.2 The positional relationship between the injected beam and the stored beam orbit. Numbers without units in the figure represent millimeters.

6.3 Magnets for beam injection

The specifications of the electromagnets for beam injection are given in Table 6.2. The kicker magnets (BP1 to BP4) have C-shaped laminated cores of 0.1 mm thick silicon steel sheet. To assure the closed orbit bumps free of beam fluctuation at the moment of the injection disturbing the experimental users, the identity of the magnetic field waveform of the four kicker magnets is the key. For a better magnetic field identity, each pair of the two upstream (BP1, BP2) and the two downstream (BP3, BP4) kickers are driven respectively by one high-precision pulsed power supply with solid-state switching devices. The vacuum chambers for the kicker magnets are made of ceramics. The inner surfaces are coated with a metal like Ti to reduce the coupling impedance. The shape and thickness of the coating are designed considering the influence of the eddy current on the magnetic field waveform. The DC septum electromagnets (DC SEP1 and DC SEP2) are installed in the air. They have iron cores made of silicon steel plate or electromagnetic soft iron with water-cooled coils. The in-vacuum pulsed septum electromagnet (Pulse SEP) is of an eddy current type. It has a laminated core of 0.1 mm thick silicon steel sheet placed in an ultra-high vacuum chamber made of stainless steel.

Table 6.2 Specifications of magnets for beam injection

	Kicker electromagnets (BP1、BP2、BP3、BP4)	DC septum electromagnets (DC SEP1、DC SEP2)	Pulsed septum electromagnet (Pulse SEP)
Type	C shaped	Direct drive	Eddy current
Shape	Rectangular	Sector	Sector
B(T)	0.22	1.2	1.4
Length (m)	0.22	0.4	0.5
Pulse width（μs）	3 (half-sine)	DC	10（half-sine）
Repetition (Hz)	1	DC	1
Core material	0.1mm-thick silicon steel	silicon steel or electromagnetic soft iron	0.1mm-thick silicon steel
Chamber	Ceramic chamber	Stainless steel chamber	In-vacuum

7. Beam injector linac

7.1 Overview

There are two types of electron beam injectors into the storage ring, the linac (linear accelerator) and the synchrotron. We choose the linac, because the power cost during operation is lower, a free electron laser (FEL) can be installed in the future, and the use of the high-precision, highly stable linac has been proven in SACLA [7.1] of RIKEN.

Table 7.1 Required specifications of the beam injector linac.

Items		Requirement
Beam energy	E	3 GeV
Energy spread	ΔE/E	0.16% (FWHM)
Energy stability	δE/E	< 0.2%
Bunch charge	Q	0.3 nC/bunch
Normalized emittance	βγε	< 10 mm·mrad
Bunch length	σ_z	< 5 ps (FWHM)
Pulse repetition rate	f_{rep}	1 Hz (beam injector) 25 Hz (RF conditioning)

A stable beam injection into a narrow dynamic aperture of a low emittance storage ring requires a highly stable low emittance beam. The required beam performance is shown in Table 7.2. A low emittance electron gun and a C-band accelerator are used to meet the requirements and to reduce the size of the linac. Figure 7.1 shows the arrangement of the linac and beam transport line [7.2]. The 112 m long 3-GeV linac consists of a 30 MeV electron injector, a chicane section (BC1) for beam energy measurements after the injector, and 20 C-band accelerator units, which generate a high electric field of 42 MV/m using a 50-MW klystron, an RF pulse compressor, and two 2 m long C-band accelerating structures [7.3]. A space was provided downstream of the third and fifth C-band acceleration units so that the bending magnets for the magnetic bunch compression chicane (BC2) could be installed in the future.

For stable operation of the top-up beam injection, it is important to reduce the probability of failure of the components. Especially for high-power components, we use reliable and proven components, providing sufficient margin for performance,

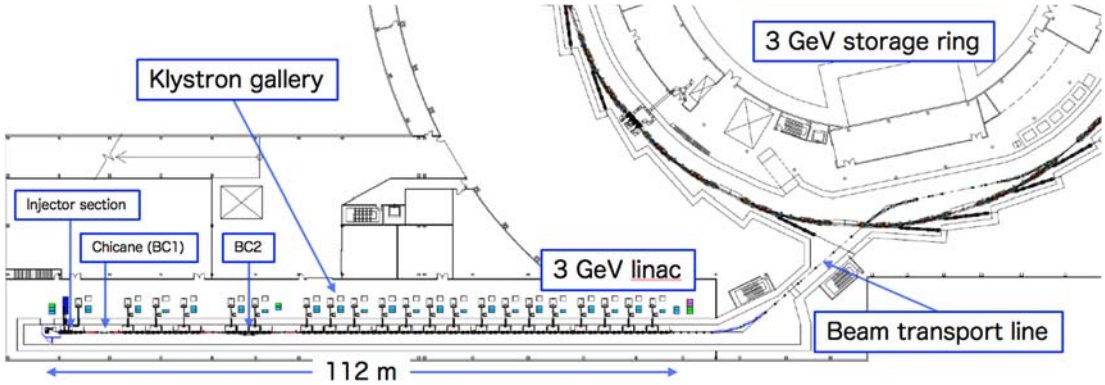

Figure 7.1 Layout of the 3 GeV linac and the beam transport line.

and allow for easy replacement in the case of failure. For usual operation, we use 18 C-band accelerator units for the beam acceleration, keeping two units as "standby". If a certain trouble happens at one of the active units, the beam operation is immediately resumed by switching the failed unit to the standby unit.

Since the maximum repetition rate of beam injection is 1 Hz, the repetition rate of the klystrons and modulators should also be 1 Hz, for usual operation. Only the case for the RF conditioning, we operate them at 25 Hz for effective conditioning. Accordingly, the electric power system and cooling water system are designed to cover 25 Hz operation, but optimized for 1 Hz operation. For the cooling water system, heat dissipation and thermal gradient at the RF cavity are negligibly small for 1 Hz operation. Therefore, we omit an individual water temperature regulation system for the RF cavity. All the accelerating structures and SLED cavities are tuned at 28 °C and the common cooling water system circulates the cooling water with a temperature of 28 ±0.1 °C. The RF amplitude and phase fluctuations caused by disturbances are highly stabilized by RF amplitude and phase feedback control of a low-power RF system using MicroTCA.4.

The magnets used at the linac are 6 magnetic lenses in the injection section, 23 quadrupole magnets for beam transport in the C-band main acceleration section, 19 steering magnets, and four bending magnets in the chicane section. The power supply for these electromagnets is the same as the digital power supply used in the storage ring to streamline the list of the backup equipment.

The beam diagnostics system consists mainly of nondestructive monitors such as current transformer (CT) and beam position monitor (BPM). All the acquired data are analyzed by the MicroTCA.4 control system and managed by the database system.

The basic lattice of the beam transport in the 3 GeV linac is FODO. Figure 7.2 shows β function, energy dispersion, and beam size. Several quadrupole magnets are installed behind the 30-MeV injector (before and after the chicane section) and in the area where BC2 is expected to be installed, for beam optics matching. In the C-band main accelerating section, quadrupole magnets are installed in every four C-band acceleration units (18 m). Figure 7.3 shows the beam profile at the end of the 3 GeV linac, estimated using a beam tracking code. The beam emittance is estimated to be less than 2 nm rad with the beam charge of 0.4 nC, and an energy spread of 0.1%.

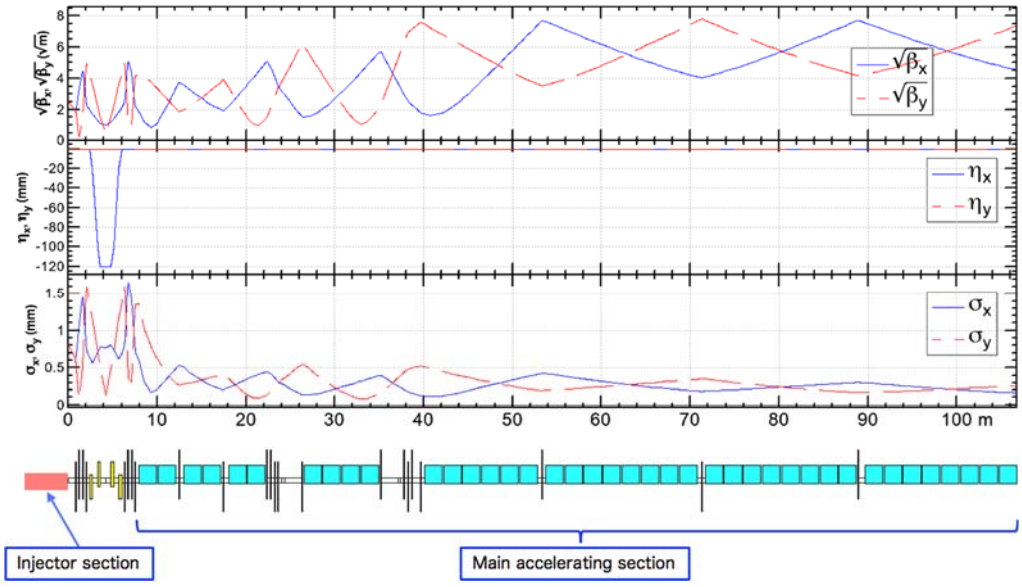

Figure 7.2 β function, energy dispersion function, and beam size in the injector linac.

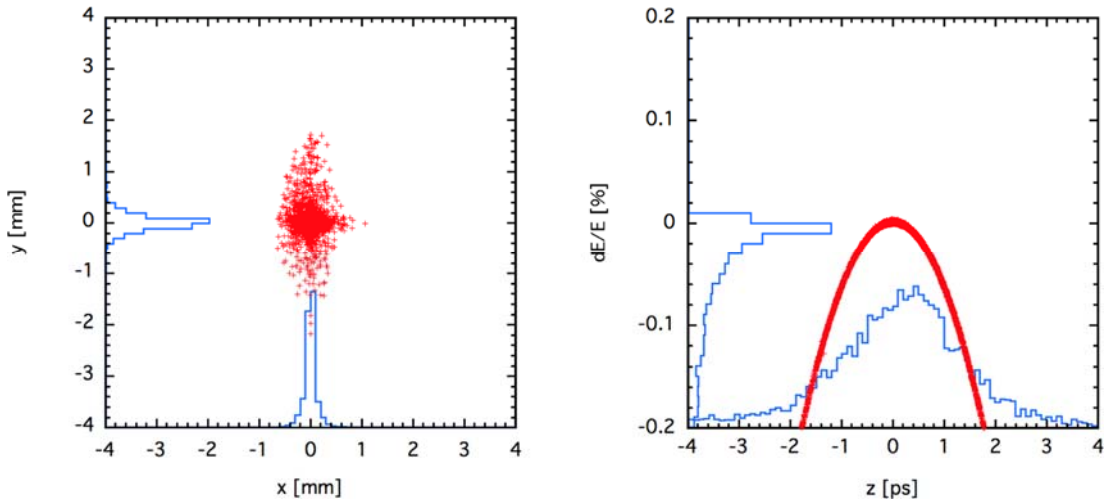

Figure 7.3 Beam size and energy-time distribution at the end of 3 GeV linac.

7.2 Electron beam injector

Figure 7.4 shows the layout of the 30-MeV injector section. The electron gun requires a charge of 0.6 nC with a normalized emittance of 5 mm·mrad. A gridded thermionic cathode (EIMAC Y-845, CPI), which is used in many accelerator facilities, is adopted as the electron source. To achieve a low emittance, the 50-kV electron gun is connected to a 238-MHz RF cavity with a minimum distance, which immediately accelerates the beam energy to 500 keV [7.4].

A low emittance 500 keV beam of 2 mm·mrad (normalized) and 0.6 nC is generated by passing through a beam collimator installed at the RF cavity exit. Subsequently, the 500 keV beam pulse is compressed by a 476 MHz subharmonic buncher (SHB) and injected into a 2 m long S-band accelerating structure. Figure 7.5 shows the results of the simulation code PARMELA for the beam performance at the exit of the S-band accelerating structure. The result shows the bunch length is compressed to 2.3 ps (FWHM) and the beam energy reaches 36 MeV.

The beam focusing system is composed of six magnetic lenses (MLs). The magnetic field strength of the magnetic lenses is adjusted to keep the optimum beam diameter and to suppress the emittance growth due to the nonlinear space charge effect.

Figure 7.6 shows the results of the normalized emittance calculation in the injector. The normalized emittance at the exit of the injector is 8 mm·mrad and the charge is 0.4 nC. The beam charge can be adjusted by the physical aperture of the beam collimator placed between the 476 MHz SHB and the S-band accelerating structure.

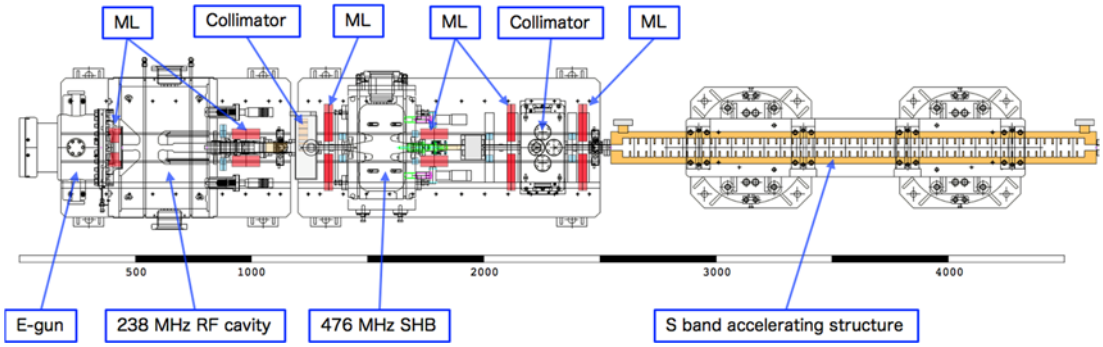

Figure 7.4 Layout of the 30-MeV injector section.

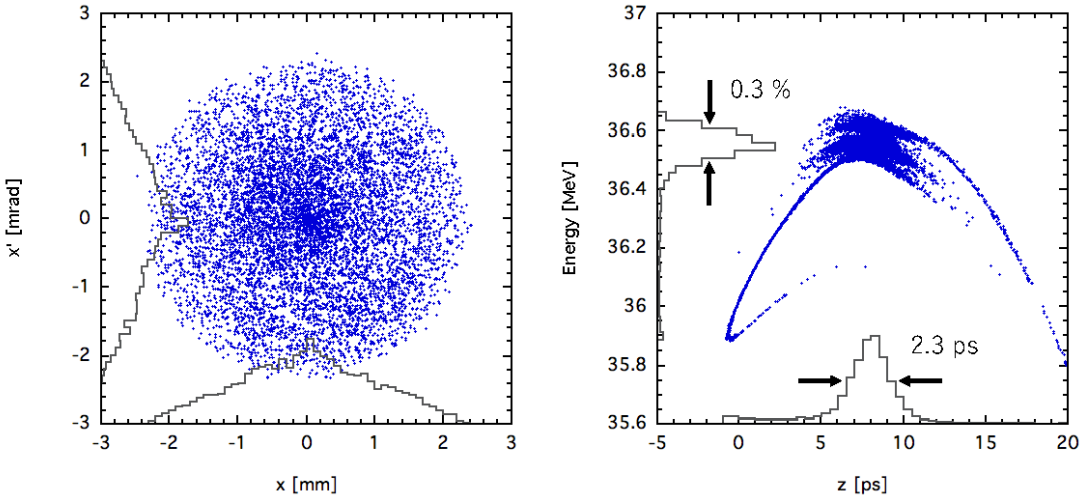

Figure 7.5 Beam size and energy-time distributions at exit of the 30-MeV injector.

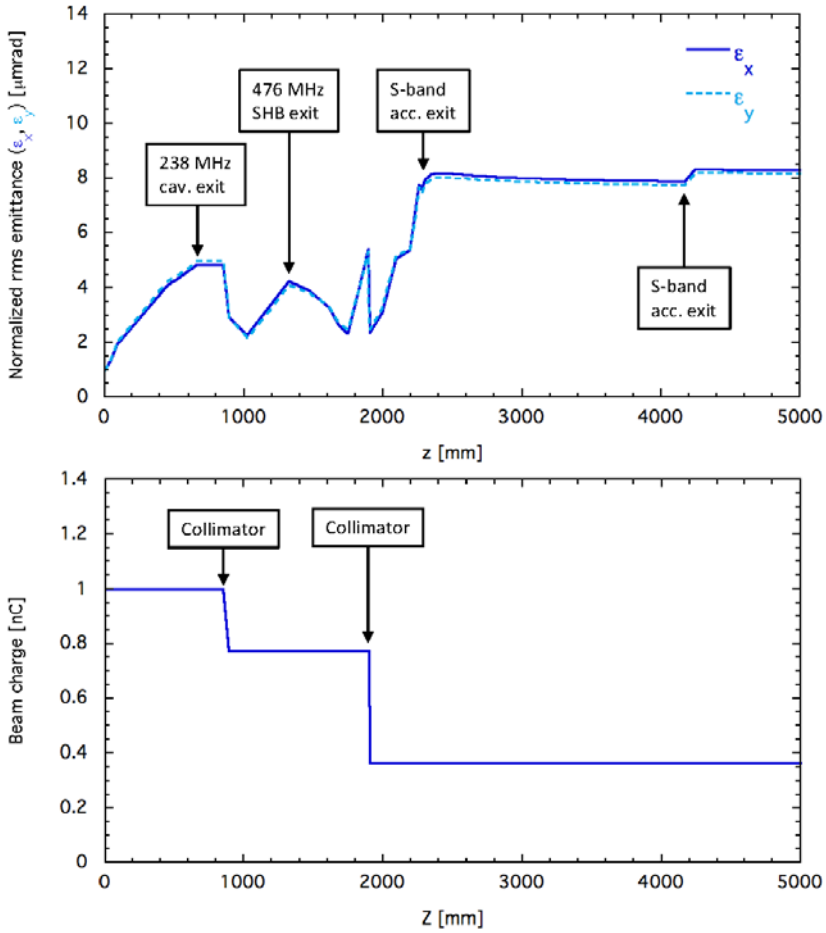

Figure 7.6 Normalized emittance and beam charge, as a function of the longitudinal position from the cathode.

7.3 Main accelerator

For the effective beam acceleration from 30 MeV to 3 GeV, we use 20 C-band acceleration units. Figure 7.7 shows the configuration of the C-band accelerator unit, and Table 7.2 shows the parameters of the main components [7.5], which is similar to the C-band accelerator system used in SACLA [7.6]. The RF power of up to 50 MW and 2.5 μs from the pulse klystron will be increased by a factor of about four by a low-loss cavity-type RF pulse compressor (SLED), and then fed into two traveling-wave-type acceleration structures. They consist of a disk-loaded structure, quasi-constant gradient type with a total length of about 2 m. It is designed to produce an average accelerating gradient of 42 MV/m when 80 MW of RF power is supplied [7.7]. The electron beam is accelerated by 168 MeV with the nominal accelerating gradient of 42 MV/m. Each klystron is driven with 350 kV, 310 A pulse power supplied by a modulator, and 300 W RF input supplied by a driver amplifier. They are remotely controlled from the upper control system through a MicroTCA.4 based low-level RF system and PLC control system installed in the control rack. A sputter ion pump is used to maintain an ultra-high vacuum inside the accelerator, RF pulse compressor, and waveguide. In addition, a ceramic waveguide vacuum window is installed between the klystron and the SLED to maintain a vacuum in the accelerator during klystron replacement. A quadrupole magnet to focus the electron beam, a steering magnet to control the orbit, a beam position monitor (BPM), and a gate valve (GV) to separate the ultra-high vacuum area is installed in each of four acceleration units (about 18 m).

Since the normal repetition frequency of the linac is only 1 Hz, the heat generated by the accelerator and RF pulse compressor is small, and the temperature fluctuations when switching between operations are negligible. The temperature of the common cooling water is controlled within 28±0.1°C. Therefore, the precise temperature regulation system of cooling water for each unit is not adopted. The temperature coefficients of the accelerator and RF pulse compressor are shown in Table 7.2. Since the main accelerator is used at the crest phase, the effect of phase change is small as long as the cooling water temperature is stable within 0.1 °C.

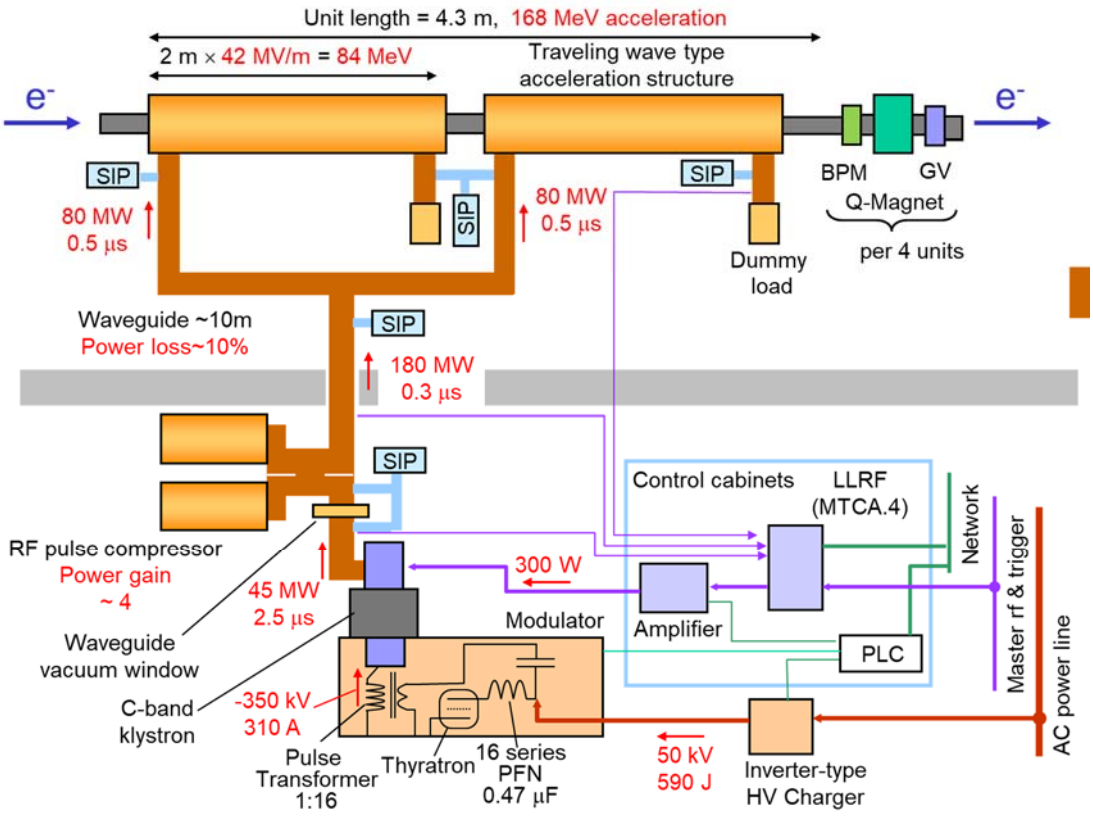

Figure 7.7 Schematic of C-band accelerator unit.

Table 7.2 Main parameters of the C-band accelerator unit

Devices	Items	Specifications
Klystron	RF frequency	5.712 GHz
	RF output power	50 MW max.
	RF pulse width	2.5 μs
RF pulse compressor (SLED)	Unloaded Q-value	185,000
	Coupling constant	11
	Power magnification factor P_{out}/P_{in} (average of filling time ~300 ns	4.0
	Thermal constant	Amplitude: 0.06%/0.1 K Phase: 1.7°/0.1 K
Acceleration structure	RF mode	2π/3 mode, Quali-constrant-gradient type traveling wave structures
	Number of cells	Regular cell 112 Coupler cell 2
	Effective accelerator length	1.994 m
	Attenuation parameter τ	0.604
	Filling time t_F	300 ns
	Shunt impedance R_{sh}	63 MΩ/m
	Nominal accelerating gradient	42 MV/m
	Temperature coefficient	Phase: 1.1°/0.1 K

7.4 Beam transport line

The electron beam accelerated to 3 GeV in the injector linac is transported to the storage ring through an 80 m-long transport line. As shown in Figure 7.8, the electron beam is horizontally deflected toward the storage ring by 42 degrees after the linac. Then the transport line goes through a radiation shield wall and crosses a photon beamline and the storage ring. Before reaching the beam injection point of the

storage ring, the electron beam is horizontally deflected twice (30 and 19.7 degrees) again and injected to the ring from the inner side using septum magnets.

The floor height of the electron beam is 800 mm at the linac and 1200 mm at the storage ring. The floor level is elevated by 200 mm at the shield wall, so the beam height of the transport line is 800 mm before the wall and 600 mm after the wall. After crossing under the photon beamline and the storage ring, whose heights are 1200 mm, the transport line is lifted up by 600 mm using two vertical bending magnets. There is a drift space of 5 m between the vertical bending magnets for the transport route of an insertion device.

Figure 7.9 shows the beam optics of the transport line. All the bending magnets have water-cooled coils, and each horizontal deflection is made by a four-bend achromatic lattice. The quadrupole magnets have air-cooled coils except for the three magnets used in the achromatic lattice. The electron beam dump is installed downstream of the linac, and the beam is dumped by exciting only the first bending magnet. As beam diagnostics, 8 beam position monitors, 4 screens and 3 current monitors are installed along the transport line. 11 steering magnets, which are x-y combined type, are installed to adjust the beam orbit. In order to reduce the hysteresis of the steering magnets, permalloy is used for the yoke.

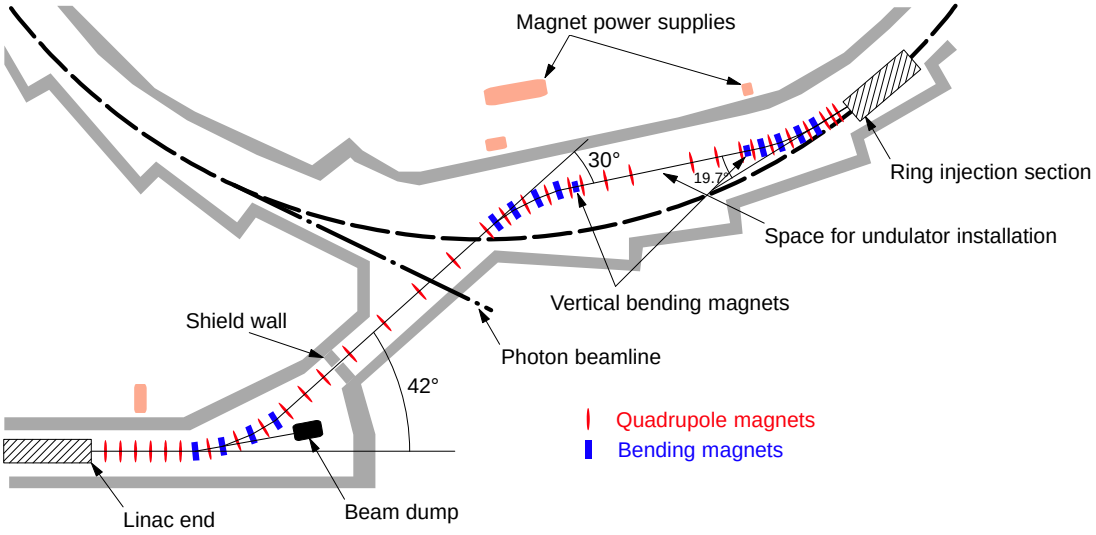

Figure 7.8 Schematic layout of beam transport line.

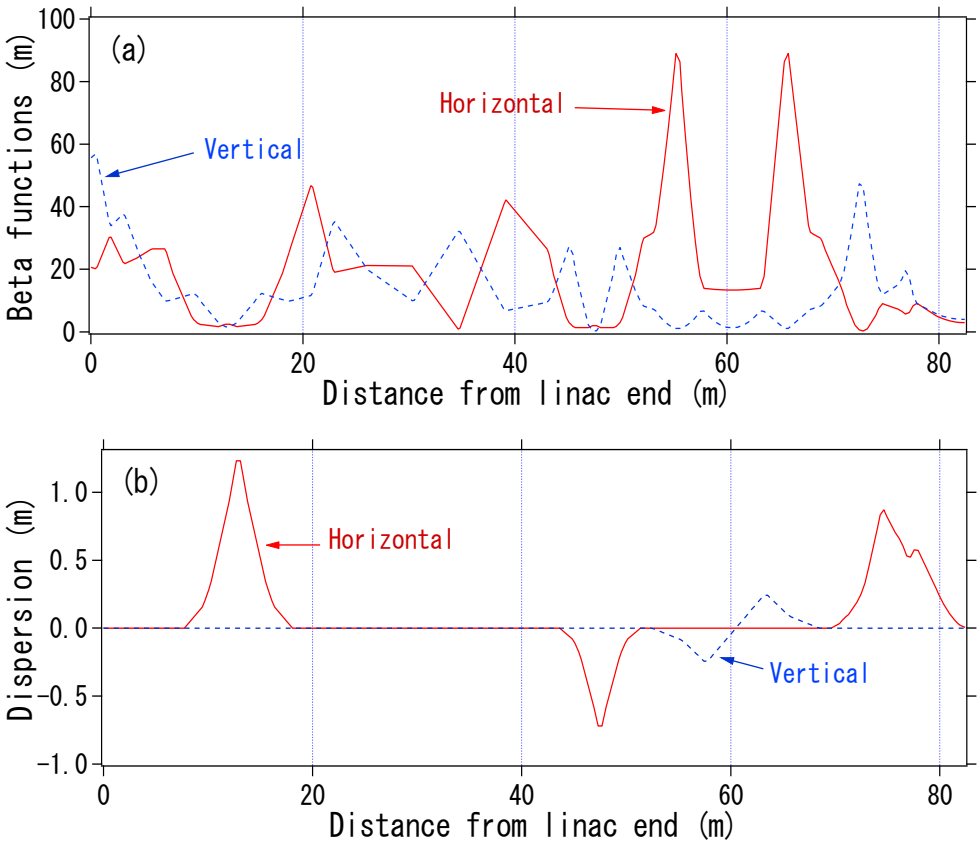

Figure 7.9 Beam optics of the beam transport line, (a)beta functions, (b)dispersion functions.

7.5 Low-level RF system

The main task of the injector linac is to inject the electron beam into the aimed bucket of the storage ring with high efficiency. It requires a high timing accuracy better than the bunch length of the ring, 6 ps, and stable beam energy better than 0.1%. To satisfy these requirements, we build a Low-Level RF system with MicroTCA.4 based modules [7.7]. The reference 238 MHz signal of the linac is generated by multiplying a rational number to the frequency of the reference 508.76 MHz signal of the storage ring. This reference 238 MHz signal is delivered to each accelerating unit through an optical link. A master trigger signal synchronized to both the 238 MHz signal and the bucket timing signal of the ring is generated using a synchronization Rear Transition Module (RTM). The master trigger is delivered through an optical link of the trigger AMC. Figure 7.10 shows a block diagram to generate the reference 238 MHz signal and the master trigger signal of the linac. At each accelerating unit, an rf signal to drive a high power amplifier or a klystron is

generated by multiplying the frequency of the 238 MHz linac reference signal. Figure 7.11 shows a block diagram of the LLRF control system for the C-band accelerating structure. The 5712 MHz signal is generated at the LO/CLK module. The 5712 MHz signal for the klystron is generated by a vector modulator (VM) to have the aimed pulse width, amplitude and phase by using a 5712 MHz RTM [7.8]. The VM signal is amplified to 800 W by using a GaN amplifier and is fed to a klystron. The pickup signals from the accelerating structure are down-converted by the RTM and are detected by a 10 channel digitizer AMC.

References

[7.1] T. Ishikawa et al., Nature Photonics 6, 540 (2012).
[7.2] T. Asaka et al., Proc. of 16th PASJ meeting, Kyoto Japan, p771, (2019)
[7.3] T. Sakurai et al., Phys. Rev. Accel. Beams 20, 042003 (2017).
[7.4] T. Asaka et al., Proc. of 29th Linea accelerator Conf, Beijing, China, p949, (2018)
[7.5] T. Inagaki et al., Proc. of 16th PASJ meeting, Kyoto Japan, p766, (2019)
[7.6] T. Inagaki et al., Phys. Rev. ST Accel. Beams 17, 080702 (2014).
[7.7] T. Ohshima et al., Proc. of 15th PASJ meeting, Nagaoka Japan, p55, (2018)
[7.8] E. Iwai et al., Proc. of 16th PASJ meeting, Kyoto Japan, p130, (2019)

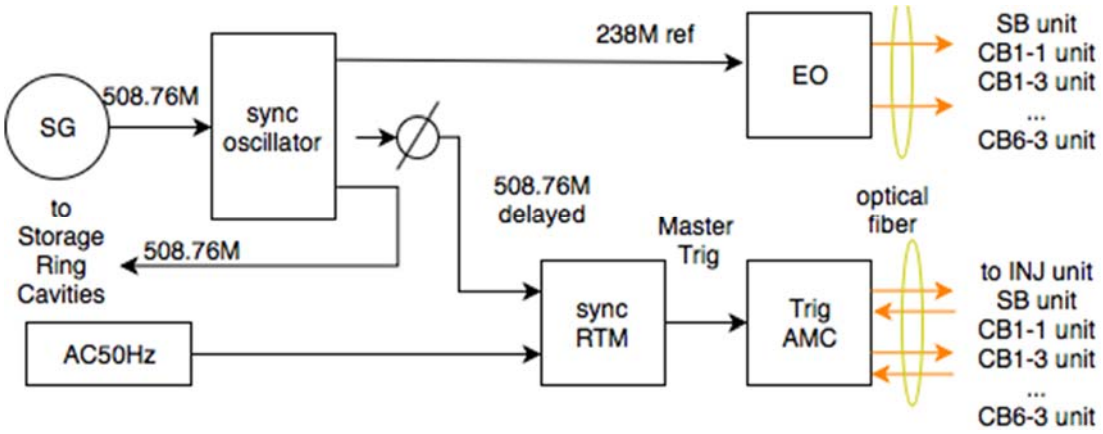

Figure 7.10 A block diagram to generate the reference 238 MHz signal and the master trigger signal of the linac.

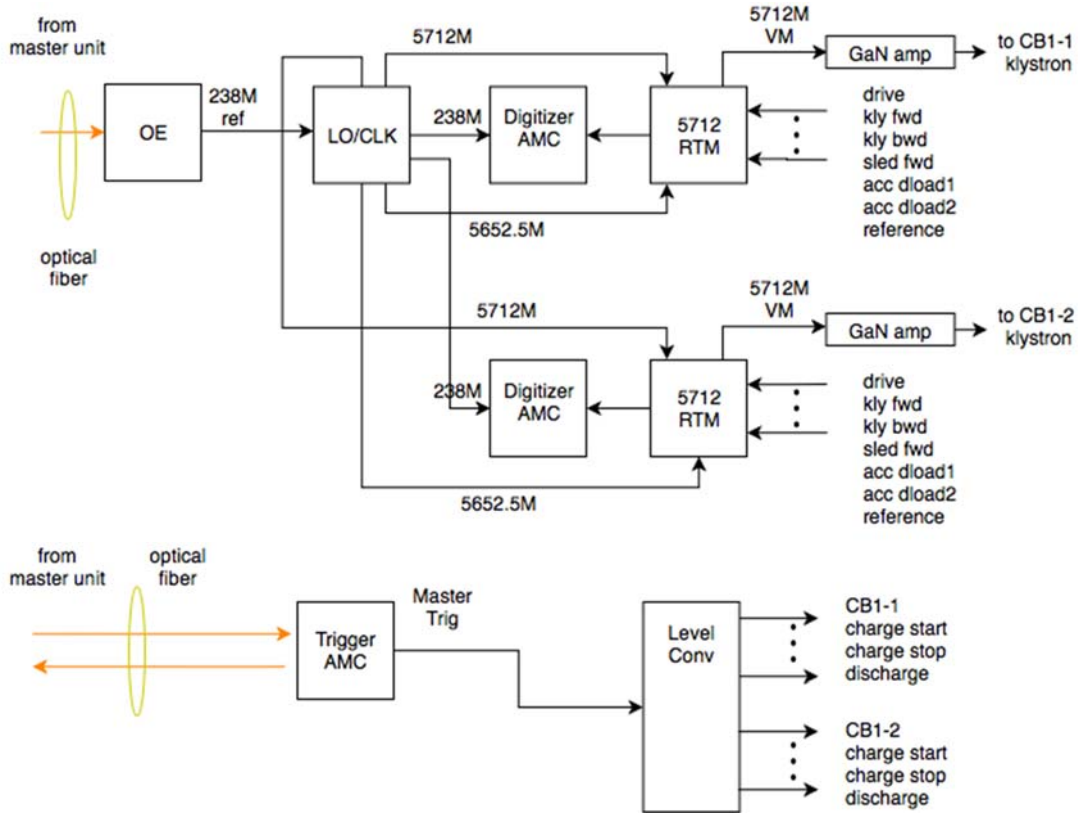

Figure 7.11 A block diagram of the LLRF control system for the C-band accelerating structure.

8. Accelerator Control System

8.1 Overview

The control framework developed by SACLA/SPring-8 is adopted as the software for the accelerator control. The framework is distributed control architecture, as characterized in the following list.

- By providing SVOC as a human-readable abstract instruction, the GUI developer does not need to know the detail of the device, and can promote the upper-level design by assembling the logic using the abstracted instructions.
- It is a control framework based on RDBMS (Relational DataBase Management System) and can maintain data integrity by managing online, archive, and parameter databases.
- Asynchronous processing using messages and network hiding can reduce the load of GUI production.
- Data collection is possible if the control system and the data collection system can be controlled by the common functions of the control system and the data collection system.
- We can visualize the data using web services.

These features ensure reliability, repeatability, stable operation and flexible control using a parameter database. The upper-level computer system used as a terminal for operation uses Linux as the operating system and provides GUI Builder and graphic libraries. The control device that controls the interlock is composed of PLC (Programmable Logic Controller) to ensure the same safety level as the hard wire. In addition, the introduction of a wiring-saving system is aimed at shortening the construction time and improving maintenance.

APIs (Application Programming Interface) are provided to obtain the operation status of the accelerator and to set the parameters of the light source to enable the user to operate from the experimental control system. The network consists of a control network and an experimental network, and the control network is separated from other networks by a firewall and constructed as an independent network. Each network will be connected to the backbone, 10G Ethernet and branch line, 1G Ethernet. The experimental network can be upgraded to the high-speed Ethernet standard (10G Ethernet for branch lines and 40G or 100 G for backbone lines) according to the future experiments. The control and experimental networks are

operated under different security policies, and communication is controlled by firewalls.

8.2 Framework of the Control System

Figure 8.1 shows a schematic view of the control system.

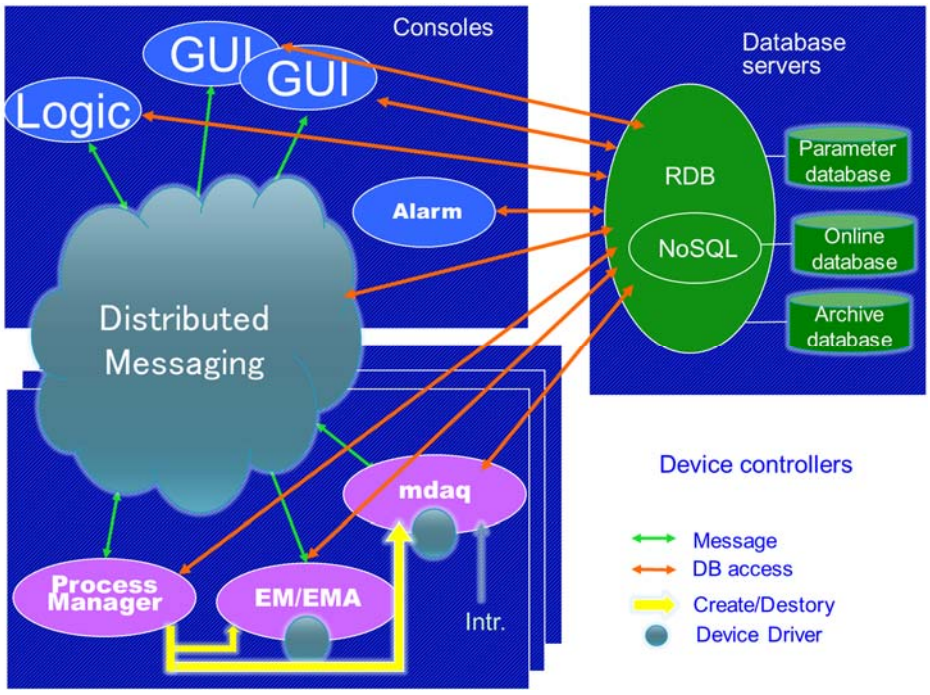

Figure 8.1 A schematic view of the control system

8.2.1 Database System and Data Acquisition

One of the features of RDBMS is that the relationship between data is maintained so that data inconsistency is difficult to occur. Another feature is the use of a language called SQL which allows for flexible searching. This is an effective tool for correlating multiple signals against archived data, for example. On the other hand, it adopts the NoSQL system database specialized in writing performance as an online database. RDBMS is adopted for the archive and parameters, and the configuration makes the best use of the features of each database. As for the parameters, the operation parameters and calibration data are handled in a unified manner, and the structure is designed to be portable and predictable by eliminating the labor for operation in text files and maintenance of hard-coded programs.

8.2.2 Data Acquisition Process

The data acquisition process (MDAQ in Figure 8.1) provides processes for periodic, synchronous and waveform data acquisition. For waveform data collection, two types of process are prepared: one that can monitor waveforms by periodically collecting them, and one that detects abnormalities and collects the waveforms before and after them. Each process is run on a host for device control (such as a PC server or MicroTCA.4) and written to the database server. Considering the delay caused by the network, the data collection process has a buffer so that the time series of the data does not change.

8.2.3 Messaging Server

Use a global message server for the exchange of messages between processes. MQTT [8.3] is adopted as the protocol for exchanging messages. This protocol was developed by IBM and standardized by ISO, etc. It is a lightweight and bidirectional protocol, and adopts the Publish/Subscribe model without queues. In case of hardware failure, it is assumed that fault-tolerant hardware or software failover will be used to minimize downtime.

8.2.4 Equipment Control Process（Equipment Manager：EM／Equipment Manager Agent：EMA）

The EM exchanges messages with the GUI for operation and operates one process on each host to control the device. For software control, we assume a latency of 100 msec or more, and for 10 msec or less, we are considering hardware support. 10 to 100 msec will be supported in consideration of process characteristics.

EMA is forked from EM for complex feedback control. The parameters used for feedback are managed by using the database management.

8.3 Equipment Control

The equipment control system controls, monitors, and collects data for vacuum equipment, RF acceleration system, magnet power supplies, beam diagnostic equipment, beam injection system, and front ends.

8.3.1 Equipment Control Platform

We plan to use MicroTCA.4 for the parts of the equipment control platform that require high-speed control (beam diagnostic system and RF acceleration control

system). MicroTCA.4, the PC servers, and network devices are monitored and tracked using standard remote management protocols such as SNMP, IPMI, etc.

8.3.2 Vacuum Equipment Control System

In the vacuum equipment control system, the PLC controls and monitors the vacuum pumps and gate valves, etc., and acquires the vacuum gauge data. In addition, each PLC is equipped with a touch panel. It can be remotely monitored to operate the equipment and monitor its condition within the storage tunnel.

8.3.3 RF Acceleration Control System

In the control system of the RF acceleration control system, the voltage, phase, frequency, temperature, timing, etc. of the acceleration cavity are set, automatically controlled and monitored by the MicroTCA.4. The high power and cooling systems are controlled by PLCs and data and other information is exchanged with the MicroTCA.4 computer via a wiring-saving system.

8.3.4 Magnet Power Supply Control System

In the magnetic power supply control system, the start/stop, current setting, and various status monitoring of the magnet power supplies are controlled by a PLC. EtherCAT [8.4] is used to control the electromagnetic power supply as a wiring-saving system.

8.3.5 Beam Diagnostic System

The beam diagnostics system controls the beam current monitor, the beam position monitor, the beam size analyzer, and the beam instability suppressor. For monitoring the beam position, MicroTCA.4, which is used in the RF acceleration system, is used for signal processing. The beam size measurement using the synchrotron radiation is carried out by capturing images acquired by a camera to a PC (or MicroTCA.4) and processing the images.

8.3.6 Device Interlock System

The device interlock system receives equipment protection interlock signals from the accelerator equipment, the insertion device and the beamline interlock system to fast beam abort the stored beam, stop the electron gun trigger for protecting the vacuum equipment.

Reference

[8.1] T. Fukui, et al., “Status of the Control System for the SACLA/SPring-8 Accelerator Complex”, Proceedings of ICALEPCS 2017, FRAPL03, Barcelona, Spain, 2017

[8.2] T. Sugimoto, et al., “Status of the Control System for Fully Integrating SACLA/SPring-8 Accelerator Complex and New 3 GeV Light Source Constructing at North Region in Japan”, Proceedings of ICALEPCS 2019, WECPL01, New York, NY, 2019

[8.3] http://mqtt.org

[8.4] https://www.ethercat.org/default.htm